Title	Detailed emissions prediction for a turbulent swirling nonpremixed flame
Author(s)	Monaghan, Rory F. D.; Tahir, Råbi; Bourque, Gilles; Gordon, Robert L.; Cuoci, Alberto; Faravelli, Tiziano; Frassoldati, Alessio; Curran, Henry J.
Publication Date	2013-12-28
Publication Information	Monaghan, Rory F. D., Tahir, Råbi, Bourque, Gilles, Gordon, Robert L., Cuoci, Alberto, Faravelli, Tiziano, . . . Curran, Henry J. (2014). Detailed Emissions Prediction for a Turbulent Swirling Nonpremixed Flame. Energy & Fuels, 28(2), 1470-1488. doi: 10.1021/ef402057w
Publisher	American Chemical Society
Link to publisher's version	http://dx.doi.org/10.1021/ef402057w
Item record	http://hdl.handle.net/10379/6849
DOI	http://dx.doi.org/10.1021/ef402057w

Detailed emissions prediction for a turbulent swirling non-premixed flame

Rory F.D. Monaghan [†,a,b,c], Råbi Tahir [d], Gilles Bourque [d], Robert L. Gordon [d], Alberto Cuoci [e], Tiziano Faravelli [e], Alessio Frassoldati [e], Henry J. Curran [b,c]

[a] Mechanical Engineering, National University of Ireland, Galway, Ireland

[b] Combustion Chemistry Centre, National University of Ireland, Galway, Ireland

[c] Ryan Institute for Environmental, Marine and Energy Research, National University of Ireland, Galway, Ireland

[d] Rolls-Royce Canada Limited, Montreal, Quebec, H9P 1A5, Canada

[e] Dipartimento di Chimica, Materiali e Ingegneria Chimica "Giulio Natta", Politecnico di Milano, 20133, Italy

Abstract

This paper describes validation of a previously-described CFD-CRN method (computational fluid dynamics - chemical reactor network) for emissions predictions for the laboratory benchmark TECFLAM S09c flame. It details CFD simulation, solution strategy, validation using, CRN generation, detailed emissions predictions and reaction pathway studies. Steady-state 3D CFD models of a 45°

[†] Corresponding author. Email address: rory.monaghan@nuigalway.ie. Tel: +353(91)494-256.

sector of the combustor, employing standard numerical techniques; steady-state k-ω SST turbulence, P1 radiation, finite-rate eddy-dissipation turbulence-chemistry interaction, and three-step methane combustion mechanism, were created in ANSYS FLUENT v14. Steady-state models were used as they are of interest to industrial researchers, who are often limited to their use by extremely complex geometries. The models differ in their handling of pressure-velocity coupling and discretization of the momentum equation. The solution which uses SIMPLE coupling and second-order upwind discretization of the momentum equation was generally found to give better results. Satisfactory agreement with experimental profiles for velocity, turbulent kinetic energy, temperature, and species mass fractions has been achieved. Some errors are seen in temperature and CO mass fractions at the highest temperatures (T > 2000 K) and are due to the fact that the highly-simplified three-step kinetic mechanism employed due to practical limitations on computational resources, underestimates CO_2 dissociation. The results compare satisfactorily with the state-of-the-art. Non-zero concentrations of CO are predicted in the external recirculation zone, which has not been achieved in previous modeling efforts. The validated solution was used as the basis to generate a CRN using the CFD-CRN method. The CFD-CRN method uses user-defined criteria to divide the CFD domain into a set of interconnected perfectly-stirred reactors (PSRs), i.e. a CRN. This CRN is then solved using detailed chemical kinetic mechanisms in the Kinetic Post-Processor (KPPSMOKE) solver. CRN size-independence studies are performed and it is determined that 5000+ PSRs were needed to adequately capture pollutant formation in the complex recirculating flow field. Validation of CFD-CRN predictions of major species show similar accuracy to steady-state CFD simulation, with improvements over state-of-the-art CFD in CO profile predictions. Satisfactory agreement with previously-published experimental NO_x contour plots is also seen. The CFD-CRN is used to study NO_x formation pathways in the swirling, turbulent environment of the S09c diffusion flame. As expected, NO_x is seen to form primarily in the high-temperature internal recirculation zone (IRZ). The prompt pathway is predicted to be of greatest importance in this area. Significant NO_x reburning is seen in the low temperature fuel-air jets

immediately adjacent to the IRZ. Overall, the prompt pathway is responsible for 77% of NO_x leaving the system, with 12% due to thermal and 11% due to N_2O intermediate.

Keywords: chemical reactor network, swirl combustor, combustion kinetics, numerical simulation, emissions modeling, fuel flexibility, gas turbines, turbulent combustion

Introduction

A number of recent factors have signaled the importance of natural gas as a major future source of energy[1,2]. These include (1) advances in unconventional gas extraction technologies, (2) the rise of intercontinental liquefied natural gas (LNG) transportation, (3) coal-to-gas switching by utility companies, (4) uncertainty about the future of nuclear energy, and (5) the need to retain fast-responding backup to increasing penetrations of intermittent renewables. This underscores the need for combustion research to enable increasing use of natural gas in the most efficient and environmentally benign manners possible. Computer-based emissions modeling techniques are used by gas turbine manufacturers and others in the field to evaluate new combustor designs and shorten the design process.

Over the past decade, combustion researchers have develop modeling techniques that leverage the advantages of computational fluid dynamics (CFD) simulations combined with chemical reactor networks (CRNs) [3,4,5,6,7,8]. Previous work by the authors introduced one such technique; the CFD-CRN method [9]. The method involves the following steps: (1) CFD simulation of a combustion system using simplified combustion models that adequately capture the velocity and temperature fields, (2) application of a set of criteria to the CFD solution that divides the CFD domain into a CRN and calculates the mass flow between reactors, and (3) simulation of the combustion system using the newly created CRN with detailed chemistry using the KPPSMOKE package[10,11]. The previous work introduced

the CFD-CRN method, its validation for emissions (CO and NO_x) predictions for the Sandia D piloted methane-air round-jet flame, and studies of the chemical pathways and physical locations of importance for pollutant formation.

The present work continues CFD-CRN validation for a more complex, more realistic combustion system, the TECFLAM S09c confined swirling turbulent methane diffusion flame. This paper describes CFD simulation, CRN generation, validation of CFD and CFD-CRN approaches, emissions predictions and studies of pollutant formation pathways. This paper is organised as follows: description of the case to be modeled, including available experimental data, description of the CFD modeling techniques employed, description of the CFD-CRN method, validation of both models, studies of pollutant (CO and NO_x) formation, including locations and pathways of importance, and discussion of results obtained.

Modeling Case

Description

The TECFLAM cooperation is a partnership, which includes Deutsches Zentrum für Luft- und Raumfahrt (German Aerospace Centre, DLR) Stuttgart, University of Karlsruhe, University of Heidelberg, and Technische Universität Darmstadt (TUD). The primary motivation was establishment of an extensive experimental database for validation and improvement of mathematical combustion models. A range of geometries, conditions, and flame-types have been studied by TECFLAM, which are typically classified according to the thermal load, the amount of swirl, flame confinement and extent of fuel-air premixing.

The S09c case consists of a highly turbulent diffusion-mode swirling flame that operates at a 150 kW power rating under atmospheric conditions, with methane at a nominal equivalence ratio of 0.83. The burner system, a sketch of which is shown in **Figure 1**, consists of a cylindrical chamber of 500 mm diameter, with variable length (1.2–1.7 m) to permit visual diagnostics (flow visualization, speciation,

etc.). The burner configuration of interest has a theoretical swirl number of 0.9, and includes confinement and water-cooled walls. For optical access, there are four windows (100×100 mm^2). Combustion products are vented through an annular slit at the top (15 mm), with the top plate actively cooled. The injector is moved vertically within the chamber like a piston (up to 500 mm) in order to change the axial-plane of measurement[12,13]. The axial symmetry of the flame has been previously reported as being "experimentally checked and confirmed" [14,15].

While it may be considered well-studied, significant technical challenges have been reported in modeling the S09c flame[5,16,17,18]. Difficulties in modeling turbulent reactive flows are present even in simple cases, and simulation validation is exacerbated as additional elements of complexity are introduced. These elements include: capturing the wall-dominated flow and the concomitant separation phenomena within the swirl passages; the details surrounding the cooling losses at the confinement walls; the prediction of peak temperatures in the central recirculation zone, and possibly even the flame stabilization mechanism. For these reasons, successful simulation of this flame using commercial codes is presently considered challenging[5,16,17,18]. The cited literature is concerned with the turbulence–chemistry interaction, with reported chemistry models ranging from the simple one-step RANS-EBU (Reynolds averaged Navier-Stokes - Eddy break-up) to finite rate (4-step), to ACM-PDF (algebraic concentration moment - probability distribution function) models[5,17,18] to LES-CMC[19] (large eddy simulation - conditional moment closure). Success with LES-FGM[20,21] (flamelet generated manifold) has recently been reported for the premixed version of TECFLAM. Most of these advanced models are presently of academic interest, and hence not readily available for use in commercial CFD codes at the time of writing.
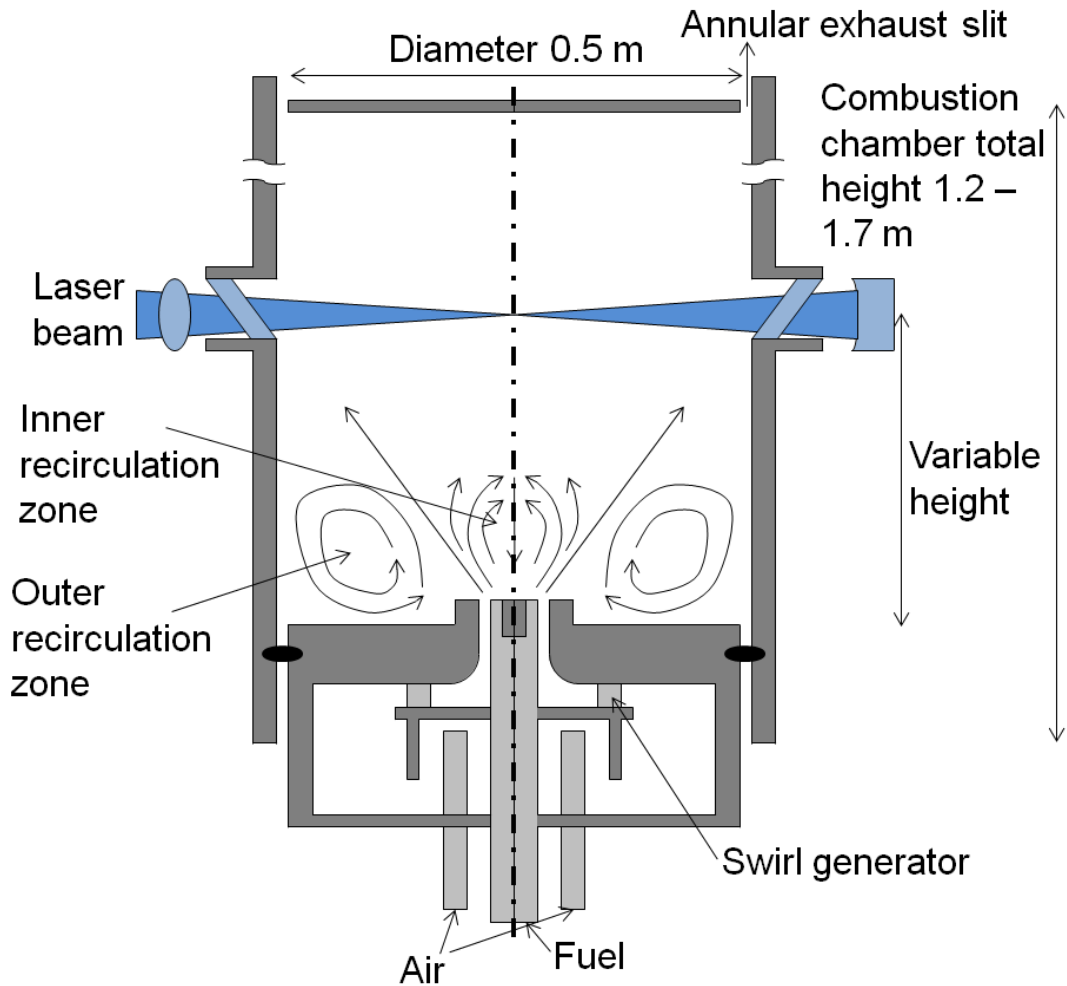
Figure 1. Sketch of the TECFLAM S09c burner and combustion chamber configuration.

Experimental Data

The existing available data consists of measurements made using various different techniques; the data available in open literature includes laser Doppler velocimetry (LDV)/Raman/Rayleigh measurements as well as results from probe samples and thermocouple measurements[14,15,22]. The temporally averaged data (mean scalar quantities) consist of radial profiles for axial (u), radial (v) and tangential (w) velocity components, turbulent kinetic energy (k), temperature (T), and mass fractions (Y_i) of CH_4, O_2, CO_2, H_2O and CO, within various axial planes, assuming flow symmetry around the central axis [23,24].

**Geometry and Boundary Conditions**

The burner geometry was reconstructed using the UG-NX6 package[25]. The geometric modeling consisted of various parameterized parts to allow variation of swirl, fuel feed and passages, confinement walls, air feed/settling chamber, etc. The swirler geometry is based on data in the open literature[26]. A cross-section of the assembled model is shown in **Figure 2**. The fuel-passage included modeling of flow through two rows of radially cut slots on an annular tube; the number and the cut-angle of these slots was adjusted to be consistent with the net flow area, while permitting modeling of a single sector—i.e., only one-eighth of the full geometry needed to be modeled (8× periodicity assumed in the flow geometry, as shown in **Figure 3**). Upstream of the swirler additional geometric features were retained to match the actual geometry. This helped predict inflow conditions for the swirl generator, without having to estimate the velocity profiles or the mass-splits at the various cylindrical faces forming the entrance to the radial swirler.

The swirler itself consists of two separate parts: a fixed block, and a moveable block. The moveable block can be adjusted to allow different amounts of gas to travel through radial and tangential passages. When all the gas travels through the radial passage, the theoretical swirl number $S_{0,th} = 0$, and when all gas travels through the tangential passage, $S_{0,th} = 1.85$. The original design was obtained from reference[12], including the description of the theoretical swirl number described by **Equation 1** for this particular flow geometry, where number of guide vanes, n = 8, maximum angular position of moveable swirl block , $\zeta_m = 15°$, outer and inner swirler radii, $R_0 = 30$ mm, $r_0 = 15$ mm, axial width of swirler channel, B = 25 mm, angular position of fixed swirl block, $\alpha = 60°$ [26]. **Figure 4** shows a plot of the theoretical value of swirl, as a function of the angular position of the moveable block. Accordingly, the angular position of the moveable block was calculated as $\zeta = 9.95°$, corresponding to the theoretical swirl number, $S_{0,th} = 0.9$ for the S09c case.
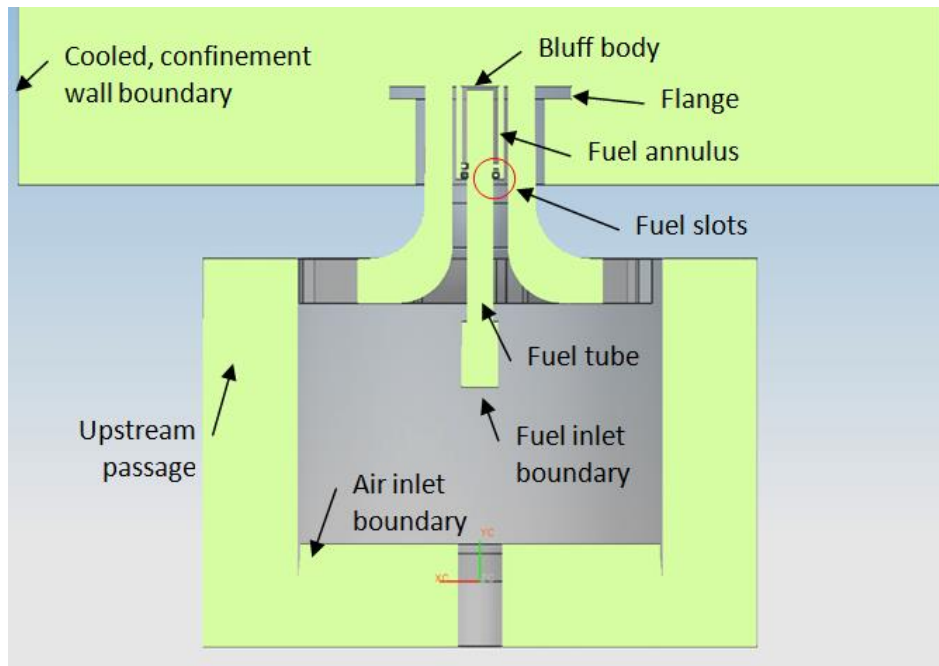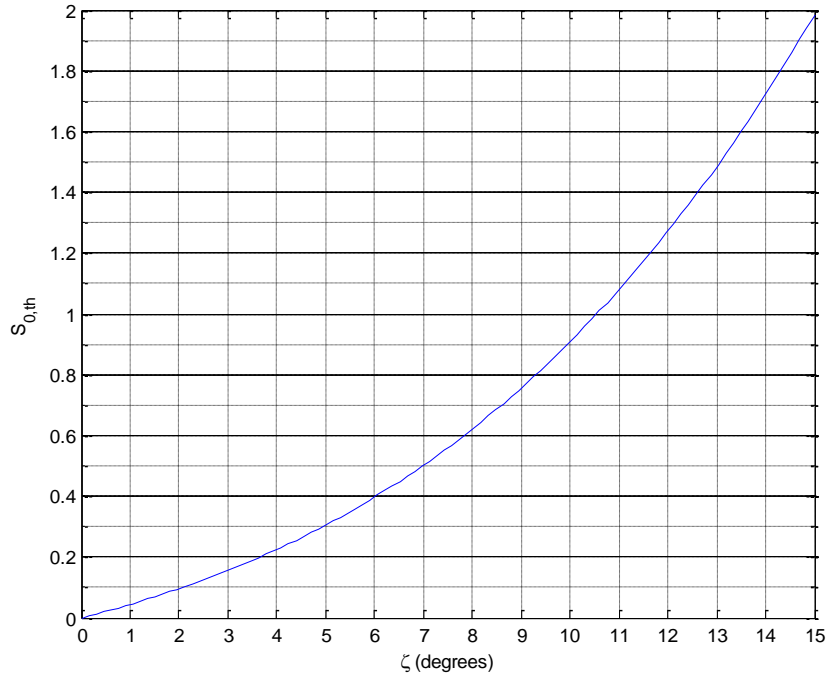
Figure 2. The assembled model, consisting of upstream, axial and swirl passages, bluff-body, and fuel-tube, etc.
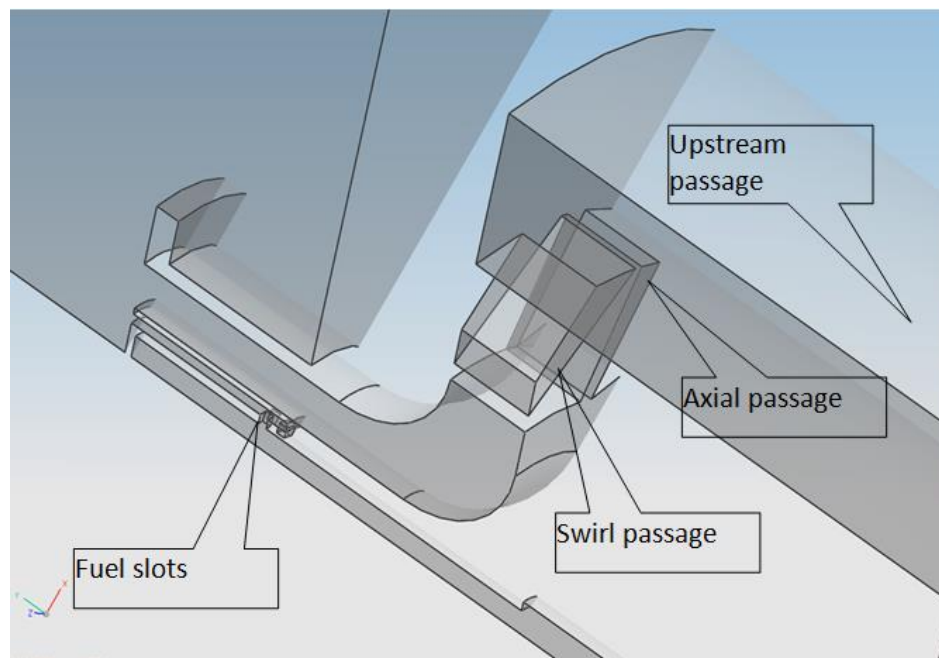
Figure 3. The periodic geometry of the simulation model, consisting of upstream, axial and swirl passages, bluff-body and fuel slots.

$$S_{0,th} = \frac{\pi}{n\zeta_m} \frac{\sin\alpha\cos\alpha\left[1+\tan\alpha\tan\left(\zeta/2\right)\right]\zeta/\zeta_m}{\left[1-\left[1-\cos\alpha\left[1+\tan\alpha\tan\left(\zeta/2\right)\right]\right]\zeta/\zeta_m\right]^2} \frac{R_0}{B}\left(1-\left(\frac{r_0}{R_0}\right)^2\right)$$ **Equation 1**

Figure 4. Theoretical swirl number as a function of the angular position of the moveable block, see **Equation 1**.

The S09c case operates at a nominal equivalence ratio of 0.833, at a thermal load of 150 kW. This corresponds to a nominal flow value of 16.7 N m^3 hr^{-1} methane and 185 N m^3 hr^{-1} air. Various authors have reported estimates for heat loss, wall temperature, and cooling water temperature. The most reliable information appears to be 80°C for the average water temperature with a net power loss from the combustor walls of 90 kW[23]. These values are used to estimate a value of convective heat transfer coefficient for CFD model boundary conditions, which are described in later sections. Qualitatively, there appears to be slight variation between the various experiments reported in the literature, and we suspect that the heat loss (wall cooling) might have been one of the more difficult items to control experimentally.

CFD Method Description

Mesh, Discretization Scheme, Solver Parameters and Resources

A hybrid structured-unstructured mesh consisting of 1.78 million cells for a 45° sector was generated using Gambit 2.4.6. Detailed views of the mesh in the (a) combustor and fuel tube and (b) air inlet and swirl passages are shown in **Figure 5**. The mesh has the following properties: structured mesh of 1 mm in the swirler (~74,000 cells), structured mesh of 0.5 mm in the fuel tube (~32,000 cells). In the combustor, the mesh is unstructured and has a smooth transition from 1 mm at the bluff body face to 5 mm with a growth factor of 1.05. In the far downstream section the unstructured mesh transitions from 5 mm to 10 mm with a growth rate of 1.1. Upstream of the swirler, the mesh is again unstructured with a smooth transition to 5 mm at the air inlet (~175,000 cells). Scalable wall functions are used and the solution was verified to be independent of mesh by comparing predicted velocity profiles with experimental data at 1 mm above the bluff body face.

This mesh was used to produce steady-state (time-independent) CFD simulations in ANSYS FLUENT version 14.0 [27]. Steady-state simulations are of particular value to industrial researchers, who are often limited by extremely complex geometries to steady-state models. Two solution methods were employed, which are henceforth referred to as Solution A and Solution B. Solution A employed full pressure-velocity coupling with second-order upwind discretization for all transport equations except momentum, which for convergence required first order upwind, while Solution B used the Semi-Implicit Method for Pressure-Linked Equations (SIMPLE) scheme with second-order upwind discretization for all transport equations. Second-order upwind discretization generally results in more accurate flow field models. The under-relaxation factors were set to 0.5 and 0.1 for pressure and momentum, respectively. Under-relaxation factors for the k-ω SST turbulence and P1 radiation transport equations were set to 0.8 and 0.98, respectively. All remaining parameters were set to unity.

The model required approximately 48 hours on 24 processors (3 GHz) to obtain a converged solution.
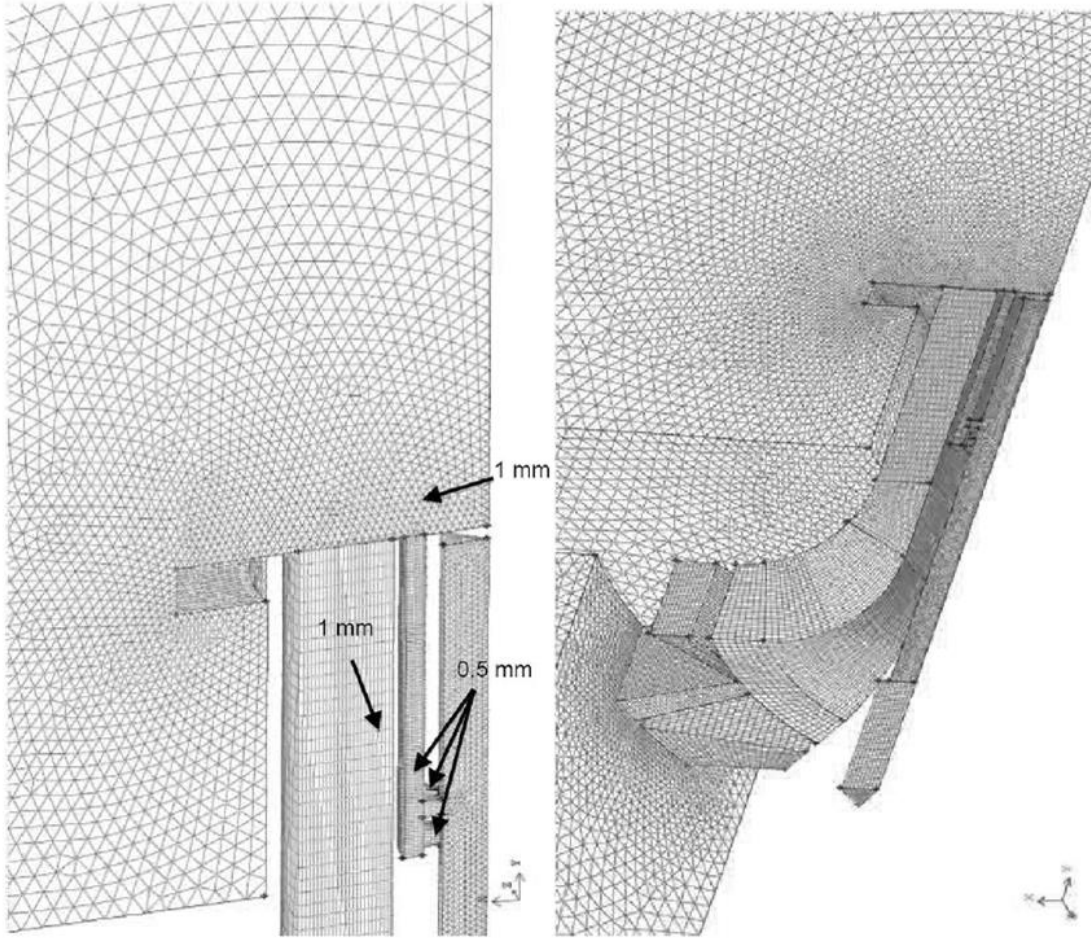
Figure 5. Views of the mesh in the (a) combustor and fuel tube and (b) air inlet and swirl passages.

Material Properties

Air and fuel were treated as ideal gases ($p = \rho RT$), with variable specific heats ($h(T) = \int c_p \, dT$). The steel walls were modeled using a density of 8030 kg m^{-3}, specific heat capacity of 502.5 J kg^{-1} K^{-1}, and thermal conductivity of 20 W m^{-1} K^{-1}.

Radiation Modeling

The P1 radiation model was used in this work[28,29]. Noticeable differences were observed between the radiation, and the no-radiation simulations. Temperature predictions made without radiation modeling were much higher than those with radiation, resulting in large over-predictions of profiles when compared to experimental data. Radiation modeling as described was therefore included.

Turbulence-Chemistry Interaction

The standard k-ω SST turbulence model was used, with $Sc_t = 0.7$. Reactions were modeled using a reduced three-step methane kinetic mechanism[30,31]. This mechanism requires the transport of five species (O_2, H_2O, CO_2, CH_4, and CO) and involves three global reactions shown in **Table 1**. Addition of the reverse CO_2 step is known to give improvement in CO prediction over the standard two-step version; however, the reaction parameters used in this study were not altered from the original values presented in references[30,31], i.e., the kinetic mechanism was not further tuned specifically for modeling of S09c. Since more than two steps are present, the turbulence chemistry interaction was captured using the eddy dissipation concept (EDC) rather than the standard finite rate eddy dissipation (FRED) model. The primary drawback in using the global chemistry scheme is that for rich mixtures, it leads to locally higher-than-true peak-temperatures, largely due to absence of sufficient treatment of endothermic dissociation; inclusion of the third step is relevant from this viewpoint as well. The benefits include relatively robust performance and reliability in terms of flame shape and stabilization, for a relatively low computational cost.

Table 1. Parameters used in kinetic mechanism

Reaction	A	E_a (kJ kmol^{-1})	α
$CH_4 + \frac{3}{2}O_2 \xrightarrow{\ 1\ } CO + 2H_2O$	5.012×10^{11}	2.0×10^5	$\alpha_{CH4} = 0.7,\ \alpha_{O2} = 0.8$
$CO + \frac{1}{2}O_2 \xrightarrow{\ 2\ } CO_2$	2.239×10^{12}	1.7×10^5	$\alpha_{CO} = 0.7,\ \alpha_{O2} = 0.25,\ \alpha_{H2O} = 0.5$
$CO_2 \xrightarrow{\ 3\ } CO + \frac{1}{2}O_2$	5.0×10^8	1.7×10^5	$\alpha_{CO2} = 1$

Boundary Conditions

The mass flow at a single far-upstream air inlet was calculated at 7.109 g/s, for a 45° sector. Pressure and temperature were 1 atm and 320 K respectively to match the available experimental data near the burner exit. The flow was assumed to be fully developed with a hydraulic diameter of 0.1 m, corresponding to the width of the annular air passage. The turbulent intensity was set to 10%.

The fuel flow, which is pure CH$_4$, was 0.371 g s^{-1}, for a 45° sector. Pressure and temperature were 1 atm and 340 K respectively to match the available experimental data near the burner exit. The flow was allowed to develop naturally through the various passages. The turbulent intensity was set to 7%, with a hydraulic diameter of 3 cm.

Heat loss through the combustor walls and into the cooling water jacket was modeled. Internal emissivity was assumed to be 10%, which is an estimate to account for the presence of quartz windows. The wall roughness was set to the default value of 0.5. The wall was assumed to be made of stainless steel, with a nominal thickness of 5 mm. A convective boundary, with heat transfer coefficient (h$_c$) of 500 W m^{-2} K^{-1}, was used to model the cooling jacket. The values of h$_c$ and cooling water flow rate were estimated based on the net heat loss (initially estimated at 60% of combustor power), the wetted area of the walls, and the requirement for no boiling to occur in the cooling jacket. As previously stated, the average temperature for water in the cooling jacket is set to 80 ºC. For Solution A, the total power loss calculated was 82.3 kW, compared to 50–90 kW estimated experimentally[18, 23]. Solution B resulted in heat loss of 88.0 kW.

The exit flow was modeled using a pressure boundary condition, at 1 atm and 1300 K, which is similar to the mean exit temperature. The backflow hydraulic diameter was set to 15 mm, i.e., the width of the annular exit channel. For radiation modeling, the internal emissivity was set to 0, which assumes external flow in the near vicinity to be hot. The mass-flow was targeted to equal the net of fuel and air at the respective inlets, and the net mass balance in the domain was verified to be zero (10^{-8} kg/s) in the steady state.

CFD-CRN Method Description

Background

The CFD-CRN (computational fluid dynamics - chemical reactor network) method was has been described in previous work by the authors[9]. CFD-CRN consists of the following steps: (1) CFD simulation of a combustion system using simplified combustion models that adequately capture velocity and temperature fields, (2) application of a set of criteria to the CFD solution that divides the CFD domain into a CRN and calculates the advective and diffusive mass flow between reactors, and (3) simulation of the combustion system using the newly created CRN with detailed chemistry using the Kinetic Post-Processor (KPPSMOKE) package developed at Politecnico di Milano[10,11]. For a detailed description of the CFD-CRN method, as well as references to other similar numerical approaches refer to reference[9]. Certain key aspects of CFD-CRN are recapitulated in this paper where necessary.

Reactor Criteria and Properties

The CFD domain is discretized into a network of perfectly-stirred reactors (PSRs) using a FLUENT user-defined function (UDF) coded in C[32]. Discretization is achieved through the comparison of cell properties with reactor criteria defined by the UDF. For a given property Z, each cell's value of Z is compared to pre-defined bins of Z. The bins by which cells are categorized determine the extent of the PSRs. Consider neighboring cells in the domain. If the two cells' properties are in the same bin as

defined by the reactor criteria, they are considered to be in the same reactor in the CRN. The bin criteria selected for this work are temperature ($\Delta T = 100$ K) and axial velocity ($\Delta u = 2.5$ m s^{-1}). This means that neighboring cells with temperatures within the same 100 K bin and axial velocities within the same 2.5 m s^{-1} bin are grouped into the same PSR. Application of these criteria produces a CRN consisting of 5551 PSRs. Note that validation of CFD-CRN is not presented here but in later sections. Such a large number of PSRs is necessitated by network size independence considerations as highlighted in **Figure 8**.

Mass-averaged properties for each reactor are calculated using Equation 2, in which ρ_i, V_i and Z_i are the density, volume and property of interest of cell i within a PSR, which consists of $N_{cell,PSR}$ cells. Contour plots of CFD cell temperature and axial velocity as well as mass-averaged PSR temperature and axial velocity are shown in **Figure 6** and **Figure 7**. These figures show the granularity that is introduced into the computational domain when 1.78 million cells (left of figures) are reduced to 5551 PSRs (right of figures).

Temporal temperature variance (σ_T^2) and root mean square temperature fluctuations (T_{rms}) for each cell are calculated for modeling the effect of temperature fluctuations on reaction rates, particularly NO_x production, as described below, using the approximate (i.e. algebraic) version of the temperature variance transport equation (Equation 14–114 in reference[27]) shown in Equation 3, where μ_t is turbulent viscosity, given by Equation 5 for RANS-based (Reynolds averaged Navier-Stokes) viscosity models, k is turbulent kinetic energy, ε is turbulent dissipation rate, ω is specific dissipation rate and C_g, C_d, C_μ are constants of values 2.86, 2.00 and 0.09, respectively, and ∇T is the magnitude of temperature gradient. Note that Equation 6 applies to the k-ω SST model only in free streams. This is applicable in the current work as T_{rms} is only of interest away from the walls. The eddy dissipation concept (EDC) model, which is used in the CFD simulation, assumes that chemical reaction occurs only in small turbulent structures, which have volume fraction ξ^{*3} as defined by Equation 7, where ν is kinematic viscosity and C_ξ is a constant of value 2.1377. Mass-averaged values for temperature variance and EDC volume fraction are

15

calculated for each PSR from individual cell values using Equation 2. The volume of each PSR available for reaction (V_{PSR}) is the product of the total volume of cells in the PSR and the mass-averaged EDC volume fraction for the PSR.

$$\overline{Z}_{PSR} = \sum_{i=1}^{N_{cell,PSR}} \rho_i V_i Z_i \Bigg/ \sum_{i=1}^{N_{cell,PSR}} \rho_i V_i \qquad \textbf{Equation 2}$$
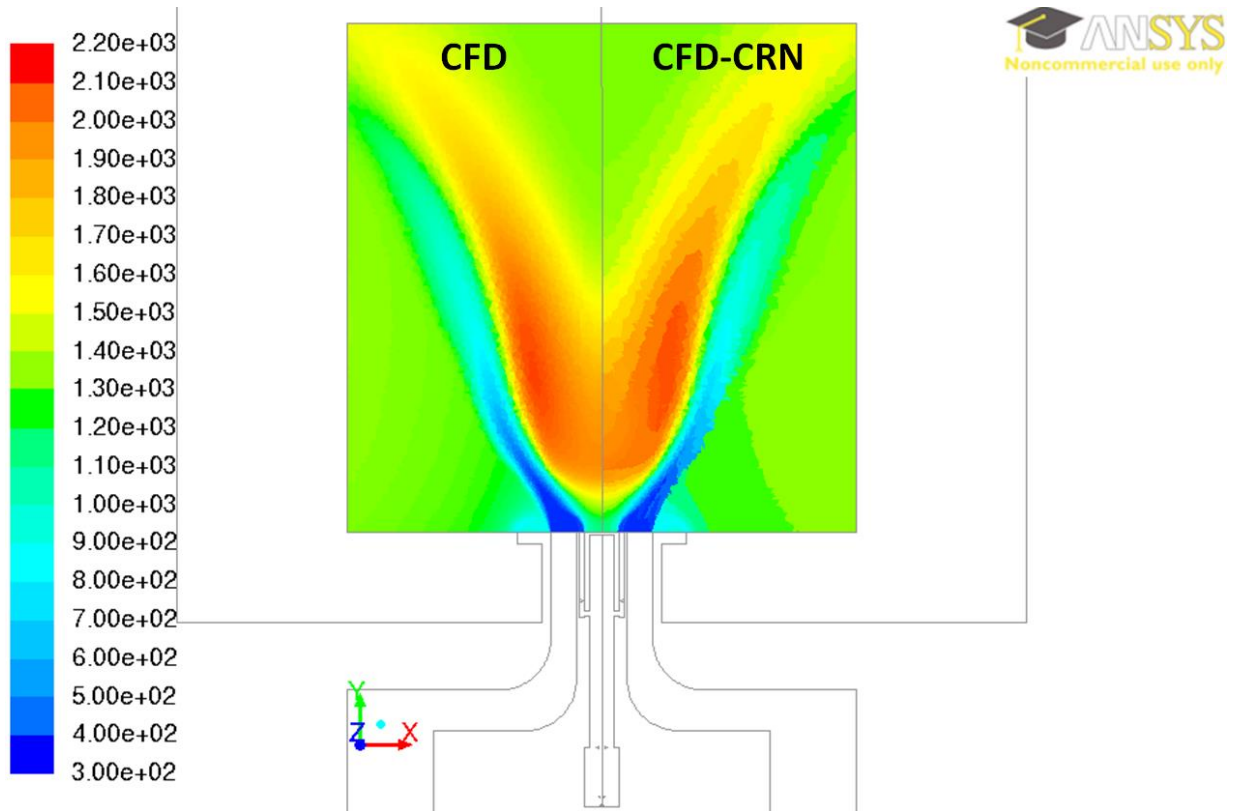
$$\sigma_T^2 = \frac{\mu_t}{\rho}\frac{k}{\varepsilon}\frac{C_g}{C_d}\left(\nabla T\right)^2 = T_{rms}^2 \qquad \textbf{Equation 3}$$

$$\nabla T = \sqrt{\left(\frac{\partial T}{\partial x}\right)^2 + \left(\frac{\partial T}{\partial y}\right)^2 + \left(\frac{\partial T}{\partial z}\right)^2} \qquad \textbf{Equation 4}$$
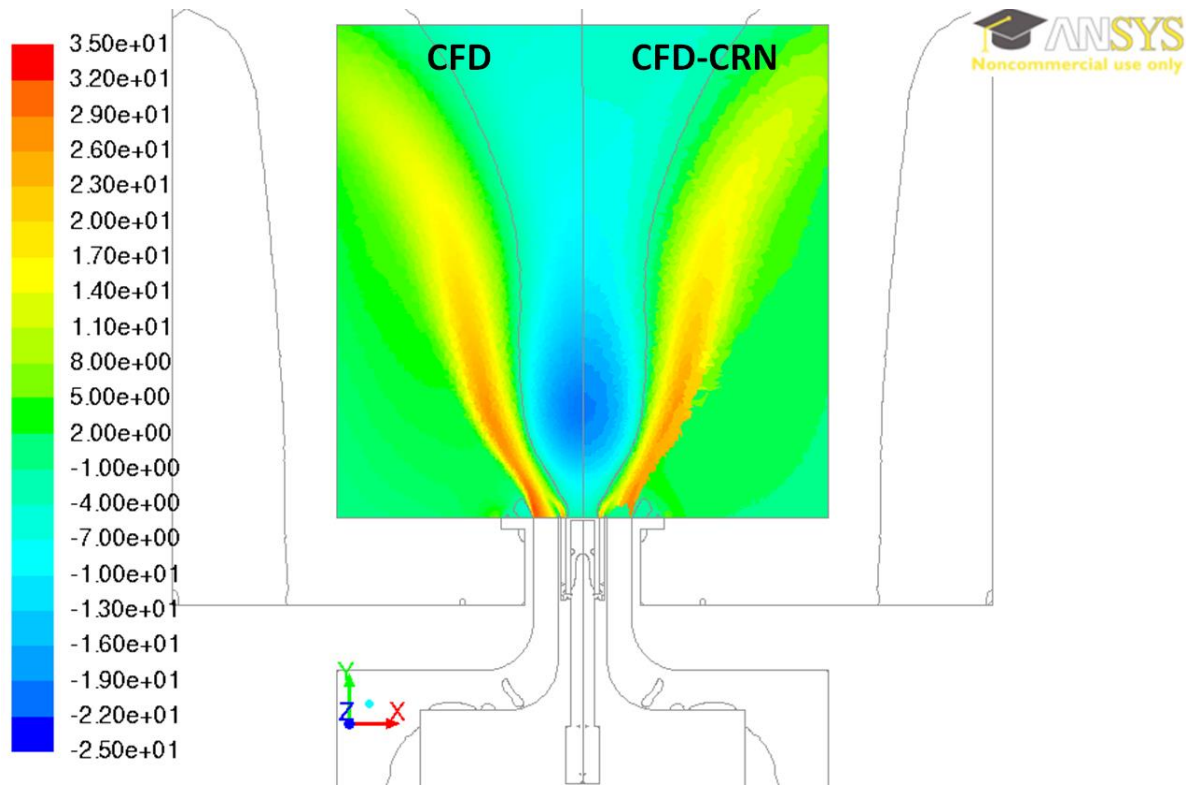
$$\mu_t = C_\mu \rho \frac{k^2}{\varepsilon} \qquad \textbf{Equation 5}$$

$$\varepsilon = 0.09 k\omega \qquad \textbf{Equation 6}$$

$$\xi^{*3} = C_\xi^3 \left(\frac{\nu\varepsilon}{k^2}\right)^{3/4} \qquad \textbf{Equation 7}$$

Figure 6. Contour plots of CFD cell temperature (in K) (left) and mass-averaged PSR temperature for

Figure 7. Contour plots of CFD cell axial velocity (in m s^{-1}) (left) and mass-averaged PSR axial velocity for 5551-reactor CRN (right). Contour of zero axial velocity (u = 0 m s^{-1}) is shown to identify recirculation zones.

Inter-Reactor Mass Flows

Two types of mass exchange are allowed between reactors; advective and turbulent diffusive. Advective mass flow between two PSRs is calculated in the UDF by summing all of the cell-to-cell mass flow rates at the boundary between the two PSRs. Turbulent diffusive mass flow between two PSRs is calculated through the indirect use of a Peclet number for turbulent mass transfer ($Pe_{m,t}$), defined in Equation 8 where u is velocity, l_{cell} is cell length-scale, defined in Equation 9, and $D_{m,t}$ is turbulent mass diffusivity, defined in Equation 10. Turbulent Schmidt number (Sc_t) is an input parameter for the CFD simulation and is set to its default value of 0.7. For each cell-to-cell advective

mass flow ($\dot{m}_{adv}$), Equation 11 can be used to calculate an equivalent turbulent diffusive mass flow ($\dot{m}_{diff,t}$). Since diffusion does not involve a bulk movement of mass, but rather an exchange of species, there are equal and opposite turbulent diffusive mass flows between cells at PSR boundaries. In a similar manner to advective mass flow, total turbulent diffusive mass flows between two PSRs are calculated by summing all of the cell-to-cell flow rates at the boundary.

$$Pe_{m,t} = \frac{u l_{cell}}{D_{m,t}} \qquad \text{Equation 8}$$

$$l_{cell} = V_{cell}^{1/3} \qquad \text{Equation 9}$$

$$D_{m,t} = \frac{\mu_t}{\rho Sc_t} \qquad \text{Equation 10}$$

$$\dot{m}_{diff,t} = \frac{\dot{m}_{adv}}{Pe_{m,t}} = \frac{\rho A D_{m,t}}{l_{cell}} \qquad \text{Equation 11}$$

CRN Solution Technique

The detailed kinetic mechanism used for this work is the C_0–C_2 portion of the C_5 mechanism developed in the Combustion Chemistry Centre (C^3) at the National University of Ireland, Galway (NUIG)[33,34]. The NO_x sub-mechanism developed at Centre National de la Recherche Scientifique (CNRS) in Orléans has been added for NO_x emissions prediction[35]. The C_0–C_2 portion of the NUIG mechanism combined with the NO_x sub-mechanism contains 103 species and 582 reactions in total.

The software used to solve the CRN with detailed chemistry is the Kinetic Post-Processor (KPPSMOKE), developed at Politecnico di Milano (Polimi) [10,11]. KPPSMOKE solves the CRN, which corresponds to a large system of non-linear equations, using a hybrid approach, combining the application of (i) successive substitutions, (ii) a false transient method and (iii) a global Newton method. This procedure is summarized in reference[9], with further references therein available to the reader.

KPPSMOKE does not solve the energy equation for each reactor in a CRN, rather it uses mass-averaged reactor temperatures ($\bar{T}$) obtained from Equation 2. This necessitates a reasonably accurate estimate of the temperature field from CFD. Turbulent combustion conditions result in temporal

fluctuations of species concentration and especially temperature, which strongly influence the characteristics of the flame and especially the formation of NO_x. The relationships between NO_x formation rate, temperature and species concentration are highly nonlinear (see Equation 12). Hence, if time-averaged composition and temperature are employed to predict the mean NO_x formation rate, significant errors will result. As a consequence, KPPSMOKE accounts for the temperature fluctuations by considering a Probability Density Function (PDF), which describes the corresponding time variation[27]. The mean turbulent reaction rate ($\tilde{r}$) is then calculated using Equation 13, where r is the instantaneous reaction rate and *p(T)* is the temperature PDF. The limits of integration are determined from the minimum and maximum values of temperature in the CFD solution. The PDF of temperature can be assumed to be a β-PDF, a clipped-Gaussian PDF or a double delta PDF. In most cases the three approaches give very similar results. In order to build the PDF of temperature, $\bar{T}$ and σ_T^2 of each reactor are required, and are calculated by the UDF and supplied to KPPSMOKE as inputs. Results are shown for cases with and without temperature fluctuation modeling.

$$k = AT^\beta \exp\left(-E_a / \Re T\right)$$ **Equation 12**

$$\tilde{r} = \int_{T_{min}}^{T_{max}} r\left(T, P, Y_k\right) p\left(T\right) dT$$ **Equation 13**

CRN Size Independence

An important part of CFD-CRN method validation is ensuring as much independence as possible of the solution from CRN size. **Figure 8** presents profiles of CFD-CRN predictions of CO mass fraction for S09c 60 mm and 150 mm downstream of the bluff body. The figure shows that CRNs consisting of 10^3–10^4 PSRs are required to reach an acceptable global level of network size independence. Computation times for the CRNs using KPPSMOKE range from 2 minutes for 114 PSRs to 4 hours 4 minutes for 7080 PSRs. The computational resource used for CRN solution is a single 2.80 GHz processor with 16.0 GB of RAM running a 64-bit Windows operating system. KPPSMOKE is also available as a parallel version [36], but this was not used for the current work. While small localized

differences are present in some high temperatures regions where reaction kinetics are fastest (see the high temperature portion of the x = 60 mm profile), the predictions of the 5551-PSR and 7080-PSR networks are globally very similar, as exemplified by the 150 mm profile. Networks consisting of 5551 or more PSRs are therefore assumed for the purposes of this work to give size-independent solutions. Validation of CFD-CRN predictions for the 5551-PSR network (calculation time 2 hours 21 minutes) against experimental data are shown in the next section. Note that **Figure 8** are representative graphs and that other areas of the flame were tested as well.
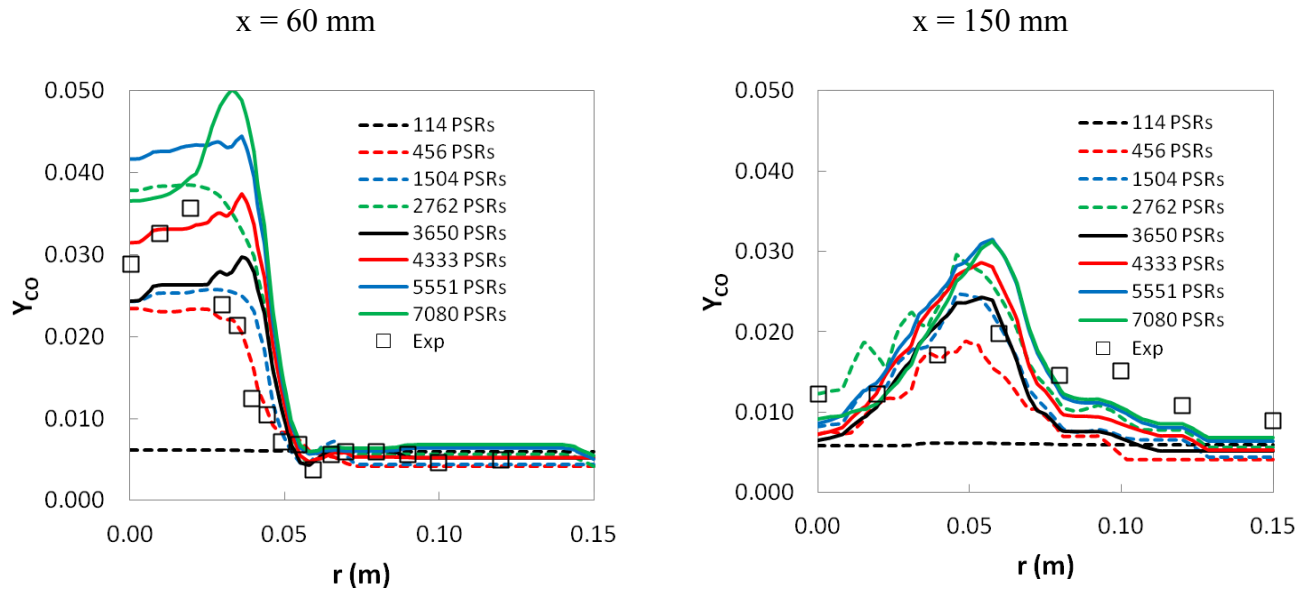

Figure 8. CFD-CRN-predicted radial profiles of CO mass fraction at 60 mm and 150 mm for CRNs of increasing size.

Validation Method

Experimental data is available for radial profiles at various standard planes, i.e., discrete heights above the burner face, as shown in **Figure 9**. In what follows, we validate our simulation results against these measurements, i.e., perform basic quantification of error in the CFD and CFD-CRN solutions. The validation exercise is presented in the form of radial profiles comparisons of experimental data and predictions from two different CFD solutions for axial (u), radial (v) and tangential (w) velocity

20

components, turbulent kinetic energy (k) and temperature (T). In addition, the analytical form of the temperature root-mean square (T_{RMS}) transport equation, obtained from Equation 3, is compared to experimentally-recorded values despite the fact this CFD simulation is steady-state. Validation is not performed for CFD-CRN predictions of these variables (u, v, w, T and T_{RMS}) since they are inputs for the CRN, not outputs. Experimental data, CFD and CFD-CRN predictions of radial profiles of mass fractions (Y_i) of CH_4, O_2, CO_2, H_2O and CO are compared. In addition the effect on CFD-CRN species predictions of modelling temporal temperature fluctuations using the statistical approach described above is examined. Measurement planes for experimental data are shown in **Figure 9**.
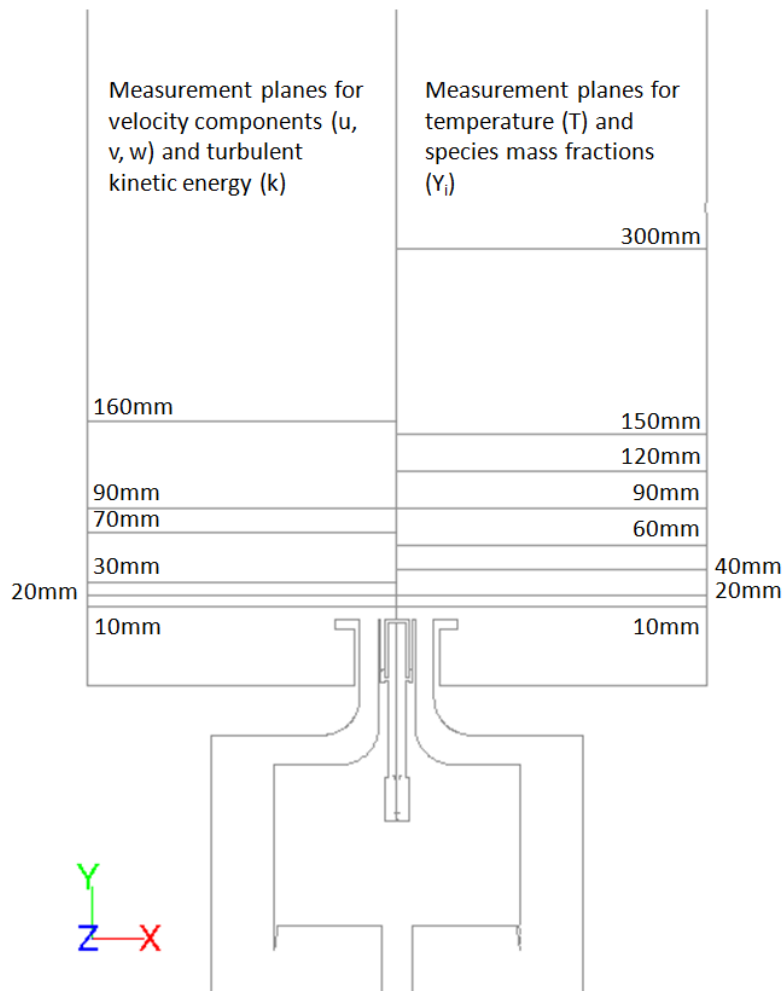

Figure 9. Measurement planes for experimentally-recorded velocity (u, v, w) and turbulent kinetic energy (k) data on left and temperature (*T*) and species mass fractions (Y_i) data on right. Numbers

21

indicate axial position relative the burner (bluff body) face.

Comparison of Two Converged CFD Solutions

Two solution methods were compared in this analysis. Solution A employed full pressure-velocity coupling with second-order upwind discretization for all transport equations except momentum, while Solution B used the SIMPLE scheme with second-order upwind discretization for all transport equations. Solution A, with coupled pressure-velocity, was found to converge only with first-order discretization of momentum. Solution B was explored in order to allow second-order discretization of all transport equations, including momentum. In order to achieve this, use of the SIMPLE algorithm for pressure-velocity coupling with pseudo-transient time stepping was necessitated.

Differences between Solutions A and B are illustrated by comparative plots of temperature contours (Figure 10) and velocity vectors (Figure 11). The primary differences in temperature fields are the ~100K higher temperatures seen in Solution A and the locations of the regions of highest temperature; on the centerline for Solution A and away from the centerline for Solution B. Greater heat loss in Solution B is a cause of the lower temperatures observed. The flame in Solution B has also lifted further from the bluff-body (burner) face. Figure 11 shows that the predicted velocity fields are qualitatively similar, although a wider internal recirculation zone (IRZ) is predicted by Solution B. Comparisons of temperature and velocity field predictions for the two solutions to experimental data are made later in this section. As will be made clear, Solution B is the preferred simulation result.
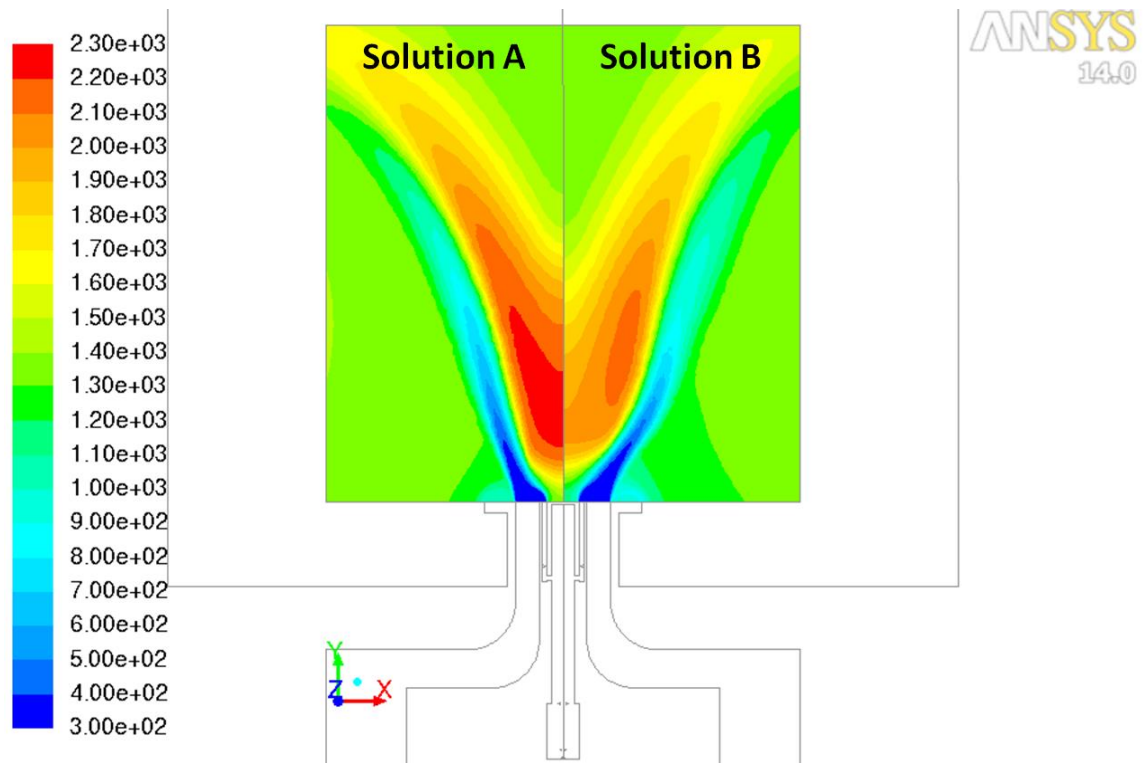
Figure 10. Temperature contour plots for Solutions A and B (in K). Compare with Figure 13.
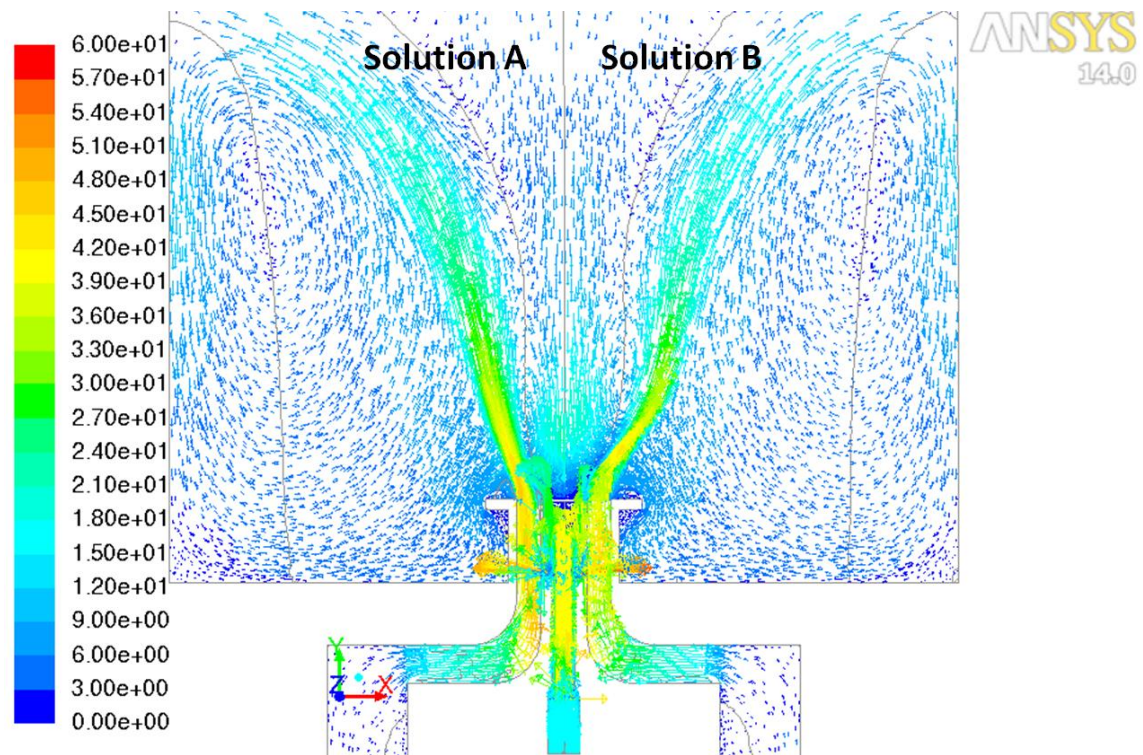
Figure 11. Velocity vector plots for Solutions A and B (in m s⁻¹). Compare with Figure 12.

**CFD-Predicted Velocity Field**

The upstream injector/swirler flow was simulated for the present study, so the comparison of the axial velocity profile at 10 mm, which is very close to the burner face, is an indicator of the performance of this work in capturing the aerodynamics associated with this complex swirling flow.

Figure 11 shows the velocity magnitude field projected onto the mid-slice for both solutions. Consider also the axial, radial and tangential velocity components shown in **Figure 12**, both for the experimental LDV measurements, as well as Solution A (dotted lines) and Solution B (solid lines). Note that close to the centreline (r = 0), the flow is directed upstream, signifying the vortex breakdown and the inner recirculation zone (IRZ) that is established under the influence of strong swirl. While not shown in **Figure 12**, as one moves away from the centreline, axial velocity flows upstream again, showing the existence of an external recirculation zone (ERZ). The swirler imparts angular momentum to the flow, and the fully developed flow exits the annular passage, which is partially separated on the inner walls. Downstream of the exit, entrainment of the surrounding non-swirling flow causes the net tangential velocity to decrease gradually with axial distance due to conservation of angular momentum. Within the incompressible framework, this drop in axial velocity leads to a positive pressure gradient in the positive axial direction. Pressure increases with distance away from the burner face, eventually recovering to the ambient wake level. The positive pressure gradient along the centreline leads to a reversed flow, known as vortex breakdown.

Moving radially outward, the velocity peaks for fuel and air inlet streams are visible. Moving further out, there is a dip caused by the wake of the flange shown in **Figure 2**. The simulation results, especially Solution B, compare favorably to those available in the open literature for the S09c flame[5,16,17], especially with respect to flame width. It should be noted that the cited works used experimental measurements of axial, radial and tangential velocity components taken at 1 mm above the burner face as boundary conditions and therefore do not consider the mixing and flow development processes taking place upstream of the burner inlet face, as this work does.

For Solution B, small deviations were observed in terms of jet width and peak axial velocity, for example at 160 mm. Overall however, the comparison of axial velocity is considered satisfactory. Referring to **Figure 12**, the jet width and peaks are adequately captured, and the ERZ is well formed, as seen in Figure 11. Similar levels of accuracy are seen for radial velocity component, with Solution B again performing better. Tangential velocity is predicted more accurately by Solution A. The discrepancy in tangential velocity component downstream indicates that the strongly swirling nature of the flame, which leads to vortex breakdown, is highly demanding for the steady k-ω SST turbulence model. With respect to turbulent kinetic energy, both solutions show lower accuracy near the burner face, which may be due to the presence of precessing vortex cores (PVCs), which cannot be modeled by steady state calculations. In previous works on this flame some difficulty in achieving convergence has been reported and it is hypothesized that it may be a result of such transient features. Nevertheless, in the present work converged solutions were obtained for both solutions A and B. As the flow develops, both solutions attain similar levels of good accuracy in predicting the locations and magnitudes of peak values.

The absence of PVCs in the steady-state modeling deserves comment: firstly, PVC is thought to be important for the S09c case, leading to enhanced mixing of the fuel and air stream; this is particularly true for the isothermal flow fields. Recent studies however indicate that this phenomenon is suppressed or at least greatly attenuated for reacting flow[19,20].
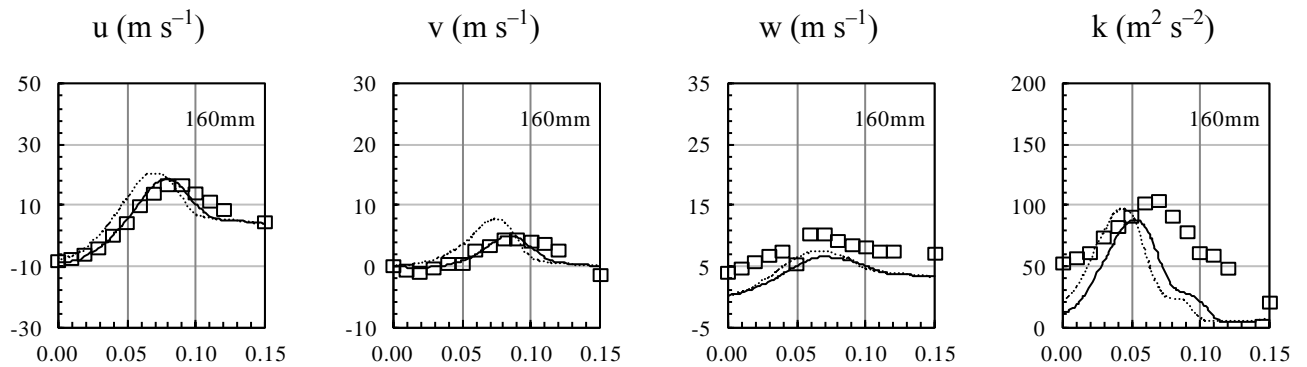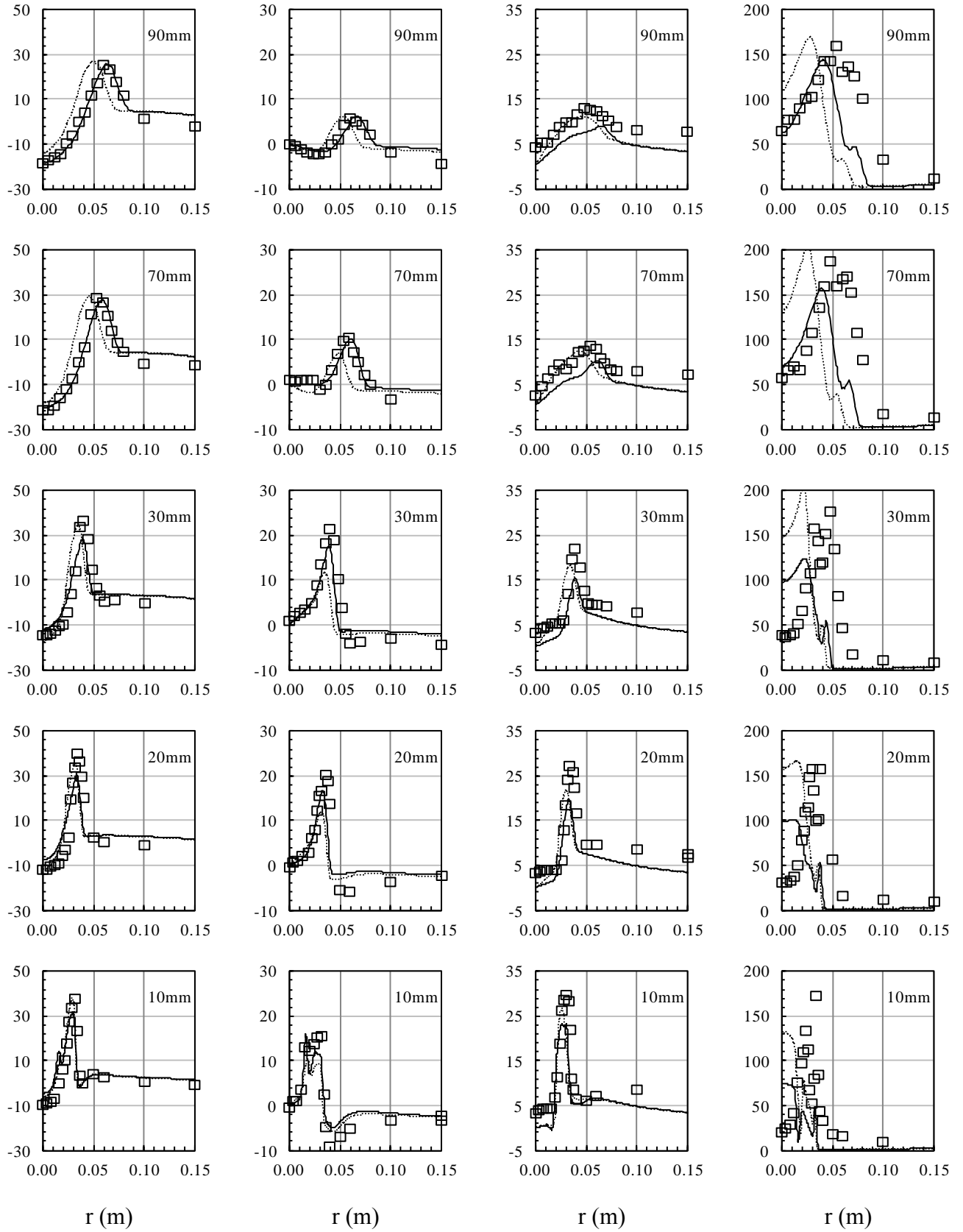
Figure 12. Comparisons of experimental and simulated radial profiles of axial (u), radial (v) and tangential (w) velocity components (in m s^{-1}) and turbulent kinetic energy (k in m^2 s^{-2}) for Solution A

(dotted lines) and Solution B (solid lines). Compare with Figure 11.

CFD-Predicted Temperature Field

From the CFD-CRN viewpoint, a certain level of accuracy in the temperature field is highly desirable. However, there exists a balance between the level of detailed chemistry employed in the CFD modelling and the associated computational cost of that detailed simulation. From a purely CRN viewpoint, it is desirable to keep the chemistry model in CFD as simple as possible, but no simpler—i.e., not so simple that the temperature field is predicted poorly. In light of this, the present results, which have been obtained with simplified 3-step chemistry, are judged to be satisfactory.

As seen in **Figure 13**, the predicted temperature field, especially that of Solution B (solid lines), compares satisfactorily to the experimental data, except in the hottest regions where the peaks are over-predicted. In these regions, the predicted temperature field is locally considered to be non-physical—i.e., the lack of detailed chemistry in the approach adopted here causes the peak temperatures to be too hot by 200–300 K. A general trend is seen that Solution A captures the temperature field very close to the burner face, but gives larger over-predictions of temperature elsewhere compared to Solution B. Due to practical limitations on computational resources, it was not possible to run the CFD simulation with more detailed kinetic mechanisms. Outside these peak temperature regions, particularly 10-60 mm from the burner inlet, the temperature field predicted by Solution B compares favourably to both experimental data as well as the state-of-the-art in published numerical work[5,16,17]. The lowest temperature trough regions indicate the cold inlet jets of air and fuel, which heat up as they travel downstream due to combustion, heat transfer and mixing with surrounding higher temperature gases. The flat, intermediate temperature regions away from the centreline are the slow moving combustion products in the ERZ, which have been cooled by heat transfer at the walls. The highest temperature regions along the centreline show the IRZ where combustion primarily occurs. As previously stated, this is where the greatest deviation from experimental results is seen, due to the highly-simplified nature of

the chemical reaction mechanism employed. Note that the shape of the temperature field predicted by Solution B, with the highest temperatures away from the centerline, is similar to that obtained by experiments for $S_{0,th} = 0.7$ and 1.4, and reported in reference[13].

Also shown in **Figure 13** are profile predictions for temporal root mean square temperature fluctuations (T_{rms}). Despite the fact that the CFD simulation described here is steady-state, estimates for T_{rms} can be obtained by using the approximate (i.e. algebraic) version of the temperature variance (σ_T^2) transport equation, shown in Equation 3. As seen in **Figure 13** the accuracy of T_{rms} predictions using the approximations outlined in this section is qualitative at best, but gives a reasonable indication of expected temperature fluctuation trends. Again Solution B generally captures the experimental trends better than Solution A.

T (K)

T_{rms} (K)
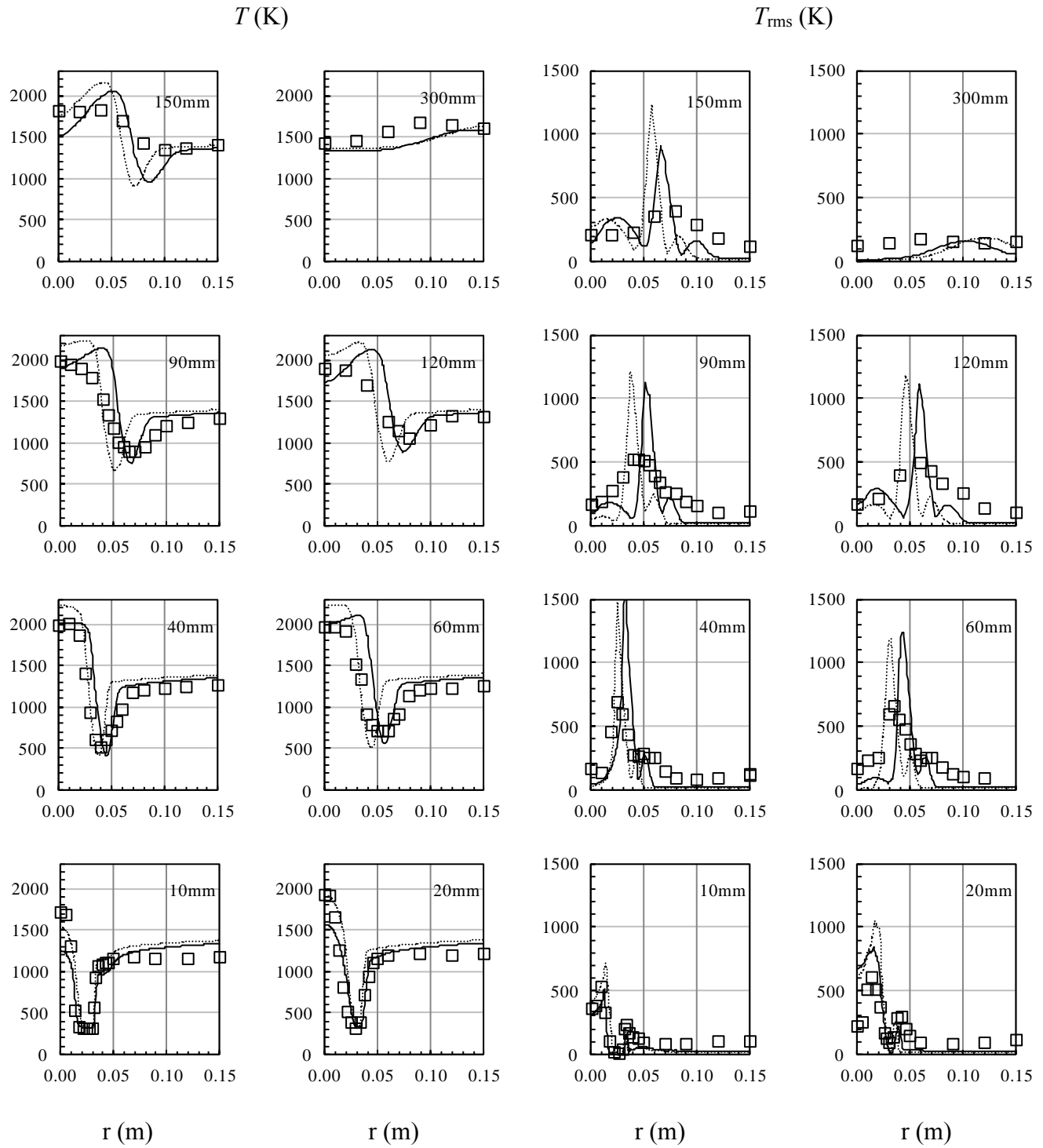
Figure 13. Comparisons of experimental and simulated radial profiles of mean temperature (T in K) and root mean square temperature (T_{rms} in K) calculated by Equation 3 for Solution A (dotted lines) and Solution B (solid lines). Compare with Figure 10.

29

CFD and CFD-CRN-Predicted Chemical Species Fields

This section covers validation of CFD and CFD-CRN predictions of chemical species. The effect of modelling temporal temperature fluctuations on species predictions using the statistical approach described above is also discussed. To focus this discussion, CFD results are limited to those obtained from Solution B. Levels of accuracy for CFD and CFD-CRN predictions of species profiles are broadly similar, as shown in **Figure 14** to **Figure 16**. For the CFD results, deviations from experimental species values coincide with temperature deviations for Solution B shown in **Figure 13**. This shows the effect of the simplified CFD chemical mechanism (**Table 1**) on the direct relationship between temperature and composition given by the Arrhenius rate expression (Equation 12). Local deviations of CFD-CRN results from experiments can be explained by two factors: (1) local deviations in CFD-predicted temperature, which is used to set local PSR temperatures, and (2) coarseness of PSRs very near the bluff body face. This coarseness is due to the fact that sharp temperature and velocity gradients are found in these locations, which may require smaller reactors. These effects are not generally seen further downstream.

Figure 16 shows a marked improvement in CO prediction when compared to the state-of-the-art modeling work for TECFLAM S09c[5,17]. Both CFD and CFD-CRN methods capture the experimental trends. CO is under-predicted by CFD in regions where predicted temperatures deviate from experimental data (see **Figure 13**), again due to the three-step chemistry model used. CFD-CRN over-predicts CO in areas where CFD-predicted temperature is over-predicted. Non-zero mass fractions of CO in the ERZ, which has been shown to be difficult to achieve[5,17], are predicted by both CFD and CFD-CRN methods. Temporal temperature fluctuations are predicted to have a minimal effect on major species profiles as seen by the similarities between the dashed and solid lines in **Figure 14** to **Figure 16**. The CFD-CRN method is deemed to be suitably validated for the purpose of pollutant formation studies.
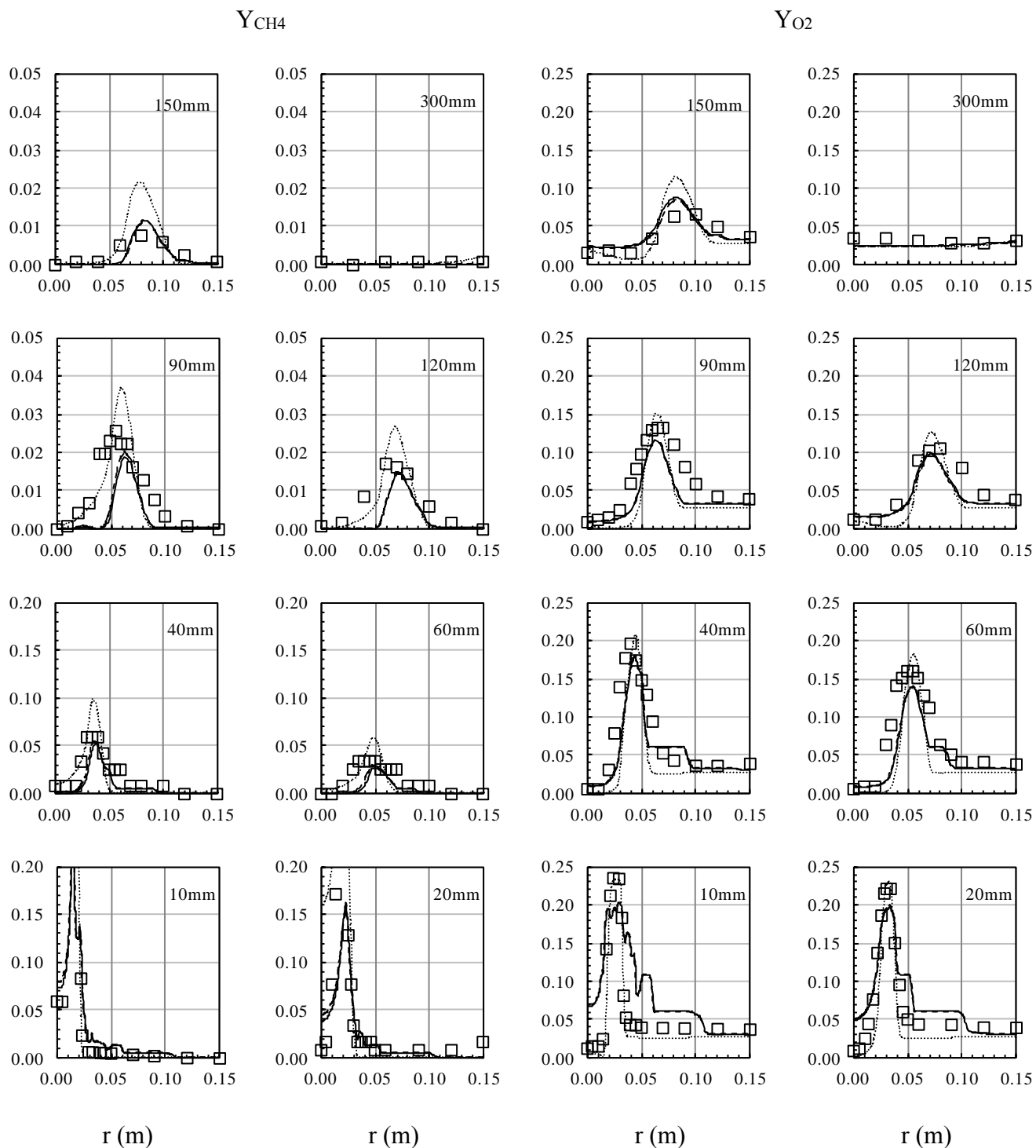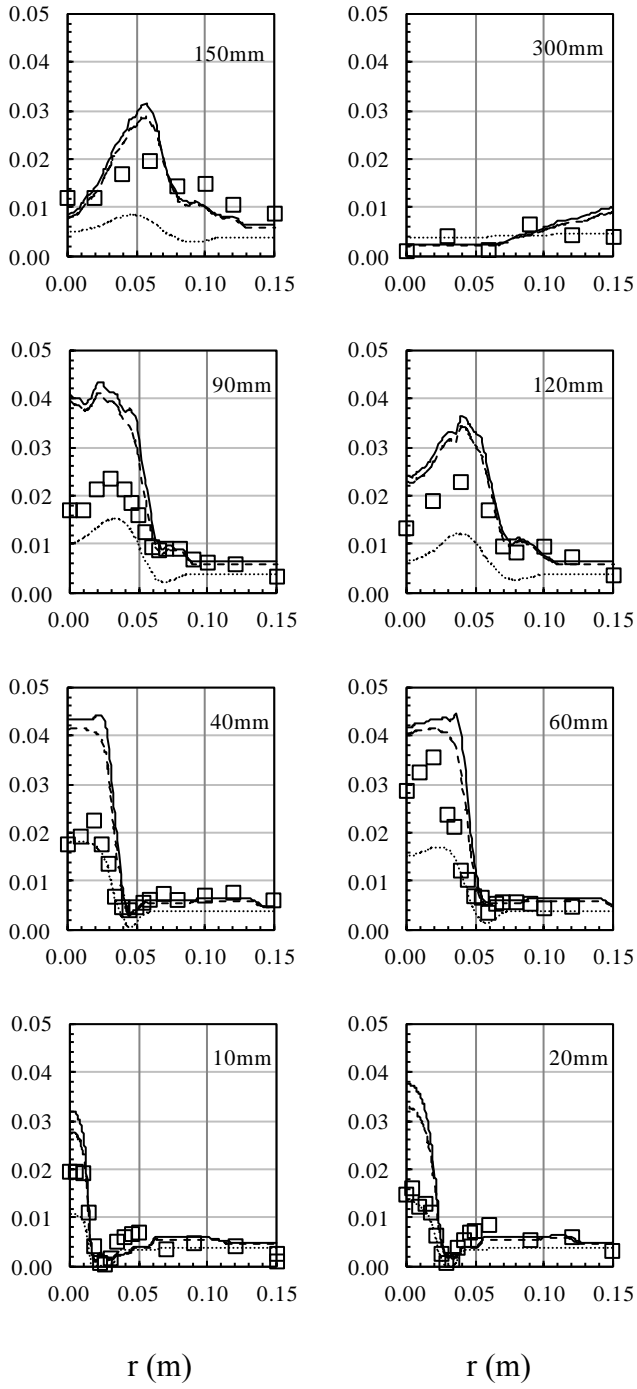
Figure 14. Comparisons of experimental (squares), CFD (dotted lines), CFD-CRN without T fluctuation (dashed lines) and CFD-CRN with T fluctuation (solid lines) profiles of CH_4 and O_2 mass fractions
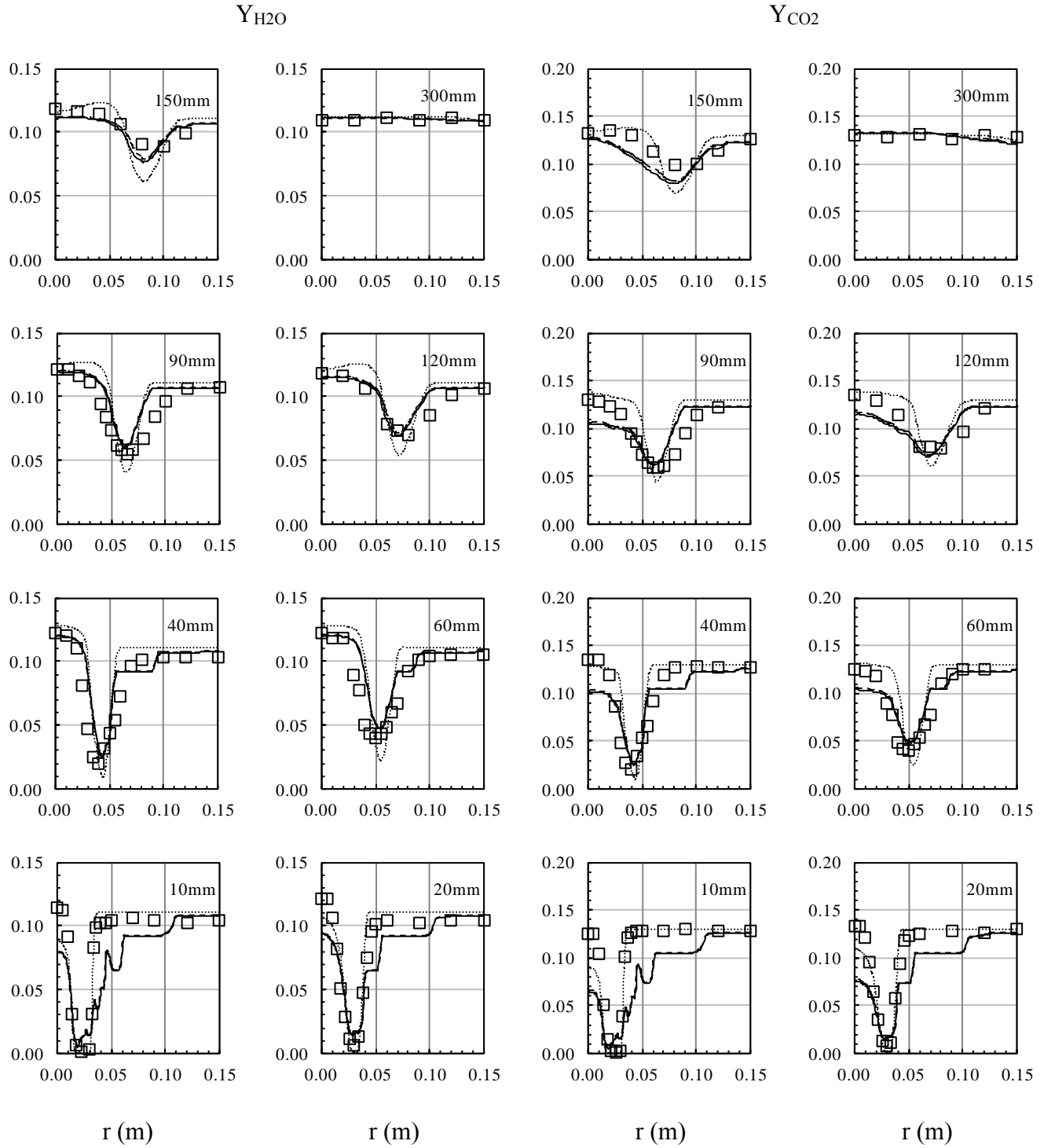
Figure 15. Comparisons of experimental (squares), CFD (dotted lines), CFD-CRN without T fluctuation (dashed lines) and CFD-CRN with T fluctuation (solid lines) profiles of H_2O and CO_2 mass fractions

Y_{CO}

Figure 16. Comparisons of experimental (squares), CFD (dotted lines), CFD-CRN without T fluctuation (dashed lines) and CFD-CRN with T fluctuation (solid lines) profiles of CO mass fraction

Results and Discussion

Formation of CO and NOx

The CFD-CRN was used to study the locations and rates of production of pollutant species CO and NO_x (defined as NO and NO_2). N_2O and HCN were also studied as they are important intermediates for NO_x formation via the N_2O and prompt pathways, respectively. **Figure 17** shows CFD-CRN predictions of CO mass fraction and CO rate of production in kg m^{-3} s^{-1} for a 150 mm × 300 mm window near the burner face. Compare the predicted values with the temperature contour plot shown in **Figure 6** and the CO validation profiles shown in **Figure 16**. CO is seen to form primarily in the shear layer where low-temperature incoming streams of fuel and air meet and mix with the high-temperature internal recirculation zone (IRZ). CO is consumed by oxidation to CO_2 in the high-temperature post-flame IRZ. Reactions of CO in the external recirculation zone (ERZ) are predicted to quench due to the cooling effect of the confining walls of the reactor.
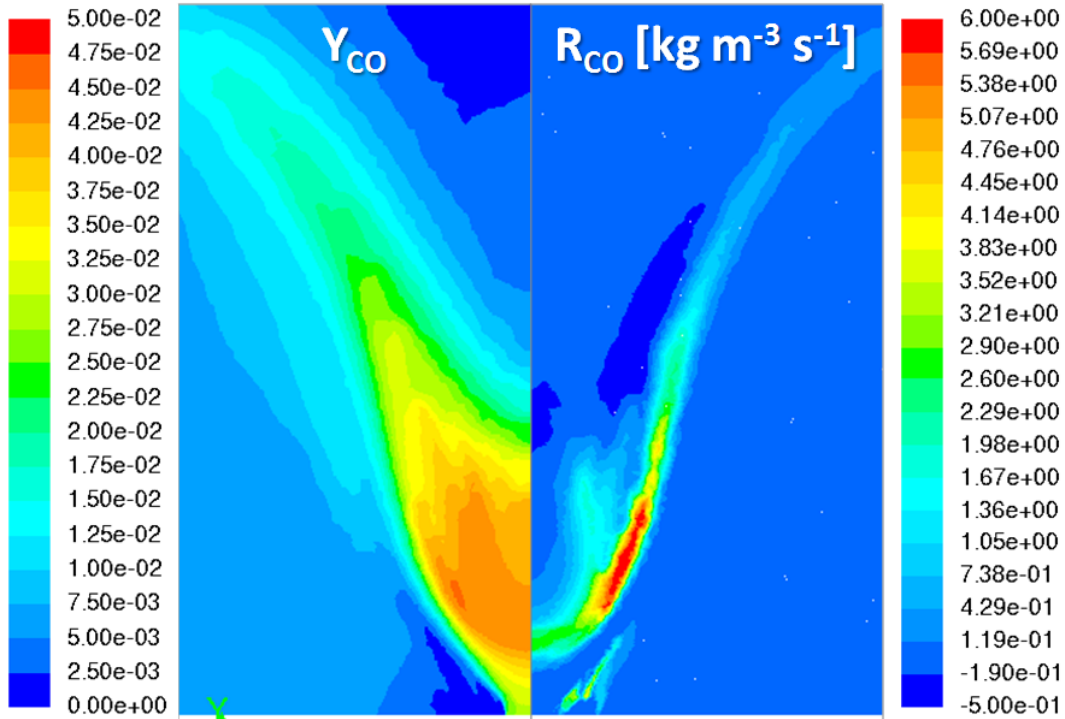
Figure 17. CFD-CRN predictions of CO mass fraction (Y_{CO}, left) and rate of production (R_{CO}, right) in kg m^{-3} s^{-1}. Refer to **Figure 6** for temperature contour plot and to **Figure 16** for Y_{CO} validation profiles.
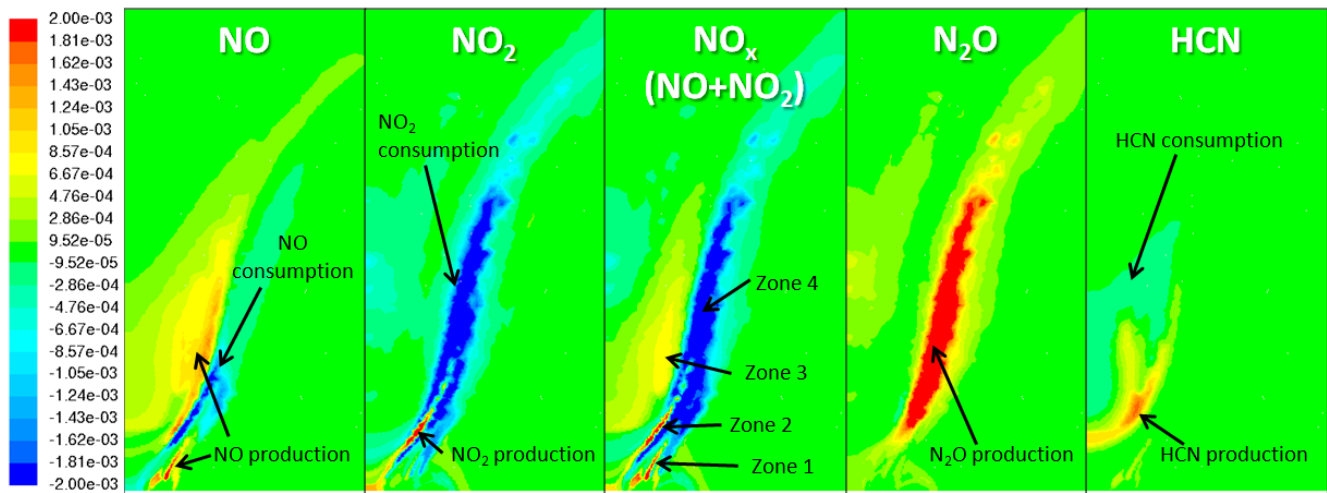
Figure 18 shows CFD-CRN predicted contour plots of concentrations of NO, NO_2, NO_x ($NO+NO_2$), N_2O and HCN in units of parts per million by mass, where $ppmm_i = 10^6 Y_i$. For clarity plots for NO_2, N_2O and HCN are multiplied by factors of 5, 10 and 5, respectively. While no experimental radial profiles of nitrogen-containing species have been reported in the literature for TECFLAM S09c with $S_{0,th} = 0.9$, a two-dimensional experimental contour plot of NO_x concentration for S09c with $S_{0,th} = 0.7$ and 1.4 is given in Figure 7 of reference[13]. The NO_x contour plot presented in **Figure 18** compares satisfactorily with the experimental data presented in reference[13].
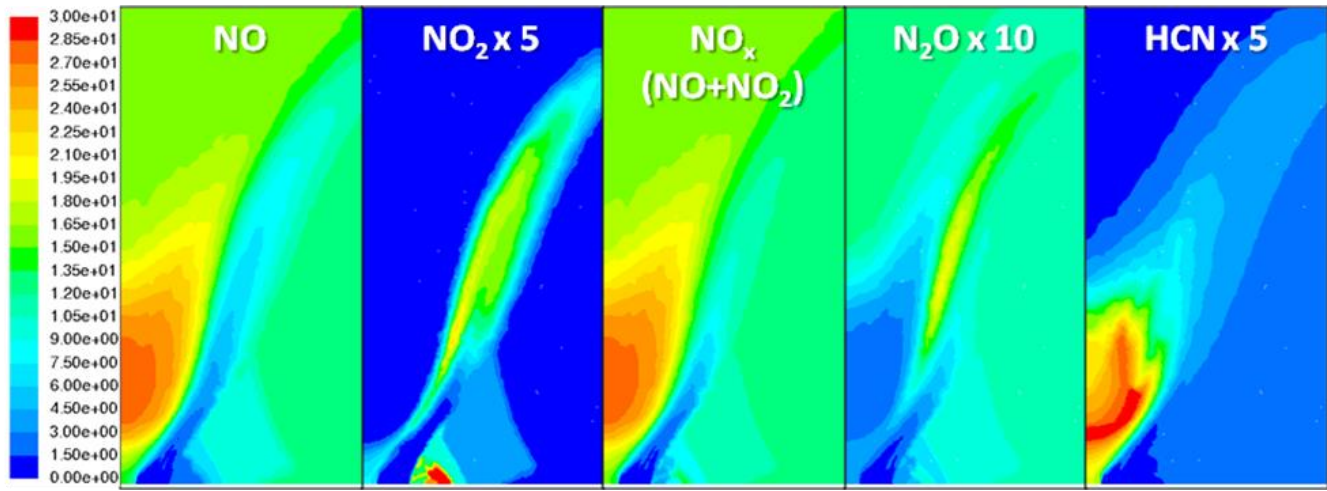
Figure 18. CFD-CRN predictions of concentrations of NO, NO_2 (×5), NO_x ($NO+NO_2$), N_2O (×10) and HCN (×5) in parts per million (by mass). Refer to **Figure 6** for temperature contour plot.

Rates of production in kg m^{-3} s^{-1} of NO, NO_2, NO_x, N_2O and HCN predicted by CFD-CRN are shown in **Figure 19**. Red indicates production, blue shows consumption and green shows no reaction. NO is seen to form in two locations; in the low-temperature region just upstream from the fuel-air inlets and on the high-temperature side of the IRZ shear layer. NO is consumed on the low-temperature side of the same shear layer. NO_2 is produced near the furthest-upstream extent of the IRZ (bottom of the figure) and is subsequently consumed throughout the intermediate-temperature jet expansion zone (JEZ) in

which fuel and air mix and react. NO_2 is predicted to form along the length of the JEZ. N_2O, a greenhouse gas, is formed rapidly in the JEZ and is not consumed to any meaningful extent anywhere in the combustor. Product gas exiting the combustor is predicted to contain 1-2 ppm of N_2O. HCN is seen to form at the high-temperature side of the IRZ shear layer and is slowly consumed further downstream in the IRZ. Now that the concentrations and rates of production of important pollutant species have been determined, the next section deals with the chemical pathways by which they are formed and the locations within the flame structure at which the pathways are important.


Figure 19. CFD-CRN predictions of rates of production of NO, NO_2, NO_x (NO+NO_2), N_2O, and HCN in kg m^{-3} s^{-1}. Refer to **Figure 6** for temperature contour plot.

NO_x Formation Pathways

NO_x is understood to form via the following generally accepted chemical pathways[37,38,39,40]: (i) thermal (or Zel'dovich), (ii) prompt (or Fenimore), (iii) N_2O intermediate, (iv) oxidation of NO to NO_2, and (v) release of fuel-bound nitrogen. An additional route, via the formation of NNH, has been postulated by Bozzelli and Dean[41], and is currently included in some, though not all, detailed kinetic schemes. The NNH pathway is not represented in the CNRS NO_x sub-mechanism[35] used in this analysis

so is not considered further in this work. The fuel in the case of S09c contains no nitrogen, so the fuel-bound pathway is also omitted from further consideration. This leaves thermal, prompt, N_2O and NO_2 pathways. The overall interaction of the pathways is illustrated in **Figure 20**, with thermal in red, prompt in blue, N_2O in magenta and NO_2 in green. The reaction of NO with fuel radicals CH_x to form HCN is known as reburning and for the purposes of this study is considered part of the prompt pathway. Note also that the N_2O pathway as defined in this work consists of two sub-pathways; reaction of molecular nitrogen with atomic oxygen and a third body (M) to form N_2O and reaction of nitrogen-containing radicals with NO to form N_2O.

The relative importance of the different NO_x pathways are determined using the procedure first described in reference[42]. This procedure involves identifying of the key reactions for each of the formation pathways and isolating in turn each of the pathways to determine their contribution to NO and NO_2 rates of production at each point in the flame. The key reactions used in this analysis are shown Table 2. By deactivating key reactions for each pathway in turn and subtracting the resulting rates of production of NO and NO_2 from the results obtained using the complete NO_x sub-mechanism, one can gain insight into the relative contributions of each pathway throughout the flame structure without dealing with each individual chemical reaction in turn. Potential sources of error in this procedure include: (i) the fact that some reactions are shared by more than one pathway, and (ii) the fact that the omission of a certain pathway may have the effect of changing the reaction rates of the remaining pathways. To address the first point, reactions shared by numerous pathways are not deactivated under any circumstances. The second potential source of error cannot be eliminated from the procedure but its effect can be quantified by comparing predictions made by the complete NO_x sub-mechanism with the sum of those made for each individual pathway. The calculated error associated with the procedure is relatively small and is shown in **Figure 22**.
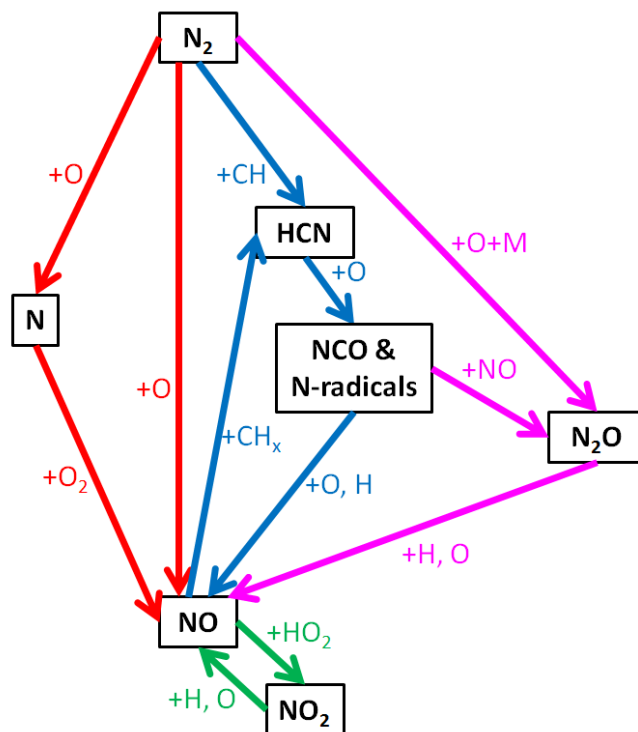
Figure 20. NO_x production pathways considered for analysis; thermal (red), prompt (blue), N_2O (magenta) and NO_2 (green).

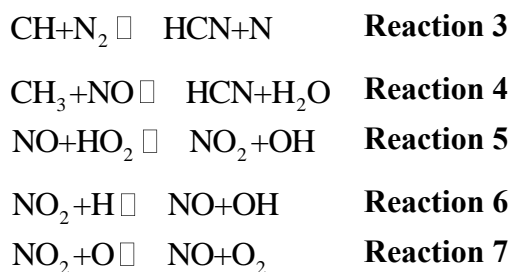**Table 2.** Key reactions for NO_x pathways under consideration

Pathway	Reaction	
Thermal	$O+N_2 \rightleftharpoons NO+N$	**Reaction 1**
	$N+O_2 \rightleftharpoons NO+O$	**Reaction 2**
Prompt	Any reaction involving HCN, NCO, HNCO, HOCN	
N_2O	Any reaction involving N_2O	
NO_2	Any reaction involving NO_2	

The results of NO_x pathway analysis are shown in **Figure 21**. The panels show local rates of production of NO (in kg m^{-3} s^{-1}) due to each formation pathway; thermal, prompt and NO_2 conversion (multiplied by 10 for clarity). As expected, the highest rates of NO production are seen in the highest-temperature regions of the IRZ. While the thermal pathway is responsible for some of this, the prompt pathway is by far the most important means of NO formation. Prompt NO production is also seen to occur at low temperature just upstream of the fuel and air inlets. NO reburning occurs on the low-

temperature side of the IRZ shear layer and is indicated by the blue area in the prompt panel in **Figure 21**. For the NO_x sub-mechanism used, HCN is a key intermediate for prompt NO and reburning via Reaction 3 and Reaction 4, respectively, which explains the production of HCN seen in **Figure 19**. The next section includes an analysis of the impact of an alternative prompt intermediate, NCN, which recent work suggests may be of greater importance than HCN. Compared to the prompt pathway, the thermal and N_2O pathways are of secondary importance, although some conversion of NO to N_2O is seen in the IRZ shear layer. Further downstream and at higher temperatures in the shear layer, NO is formed via N_2O intermediate. Conversion of NO to NO_2 at intermediate temperatures by Reaction 5 (reaction with HO_2), and subsequent re-conversion back to NO via Reaction 6 and Reaction 7 (reaction with H and O, respectively) occur throughout the shear layer.
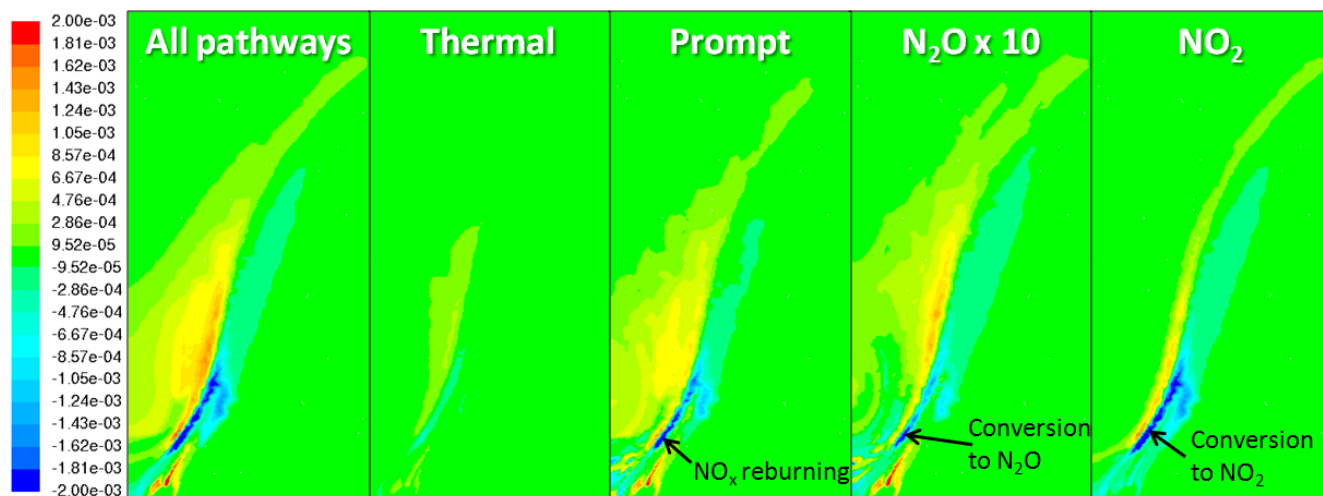
Figure 21. CFD-CRN predictions of rates of production of NO due to thermal, prompt, N_2O and NO_2 pathways in kg m^{-3} s^{-1}. Refer to **Figure 6** for temperature contour plot.

$$CH+N_2 \rightleftharpoons HCN+N \qquad \textbf{Reaction 3}$$
$$CH_3+NO \rightleftharpoons HCN+H_2O \qquad \textbf{Reaction 4}$$
$$NO+HO_2 \rightleftharpoons NO_2+OH \qquad \textbf{Reaction 5}$$
$$NO_2+H \rightleftharpoons NO+OH \qquad \textbf{Reaction 6}$$
$$NO_2+O \rightleftharpoons NO+O_2 \qquad \textbf{Reaction 7}$$

The overall contributions of each pathway to NO_x ($NO+NO_2$) concentration at a location far downstream of the flame (300 mm) are shown in **Figure 22**. Note that the NO_2 pathway is not shown since NO_x consists of both NO and NO_2, and the consumption of one leads to the formation of the other. The difference between the solid and dashed black lines in **Figure 22** illustrates the fact that there is a 7% error in post-flame NO_x concentration introduced by considering each formation pathway separately. This can be considered an acceptable level of error. The figure shows that 77% of NO_x in the post-flame region is produced by the prompt pathway, 12% by the thermal pathway and 11% by N_2O intermediate. This compares with 47% via prompt, 21% via thermal and 32% via N_2O calculated by a similar CFD-CRN analysis for the Sandia D pilot-stabilized diffusion flame[9].
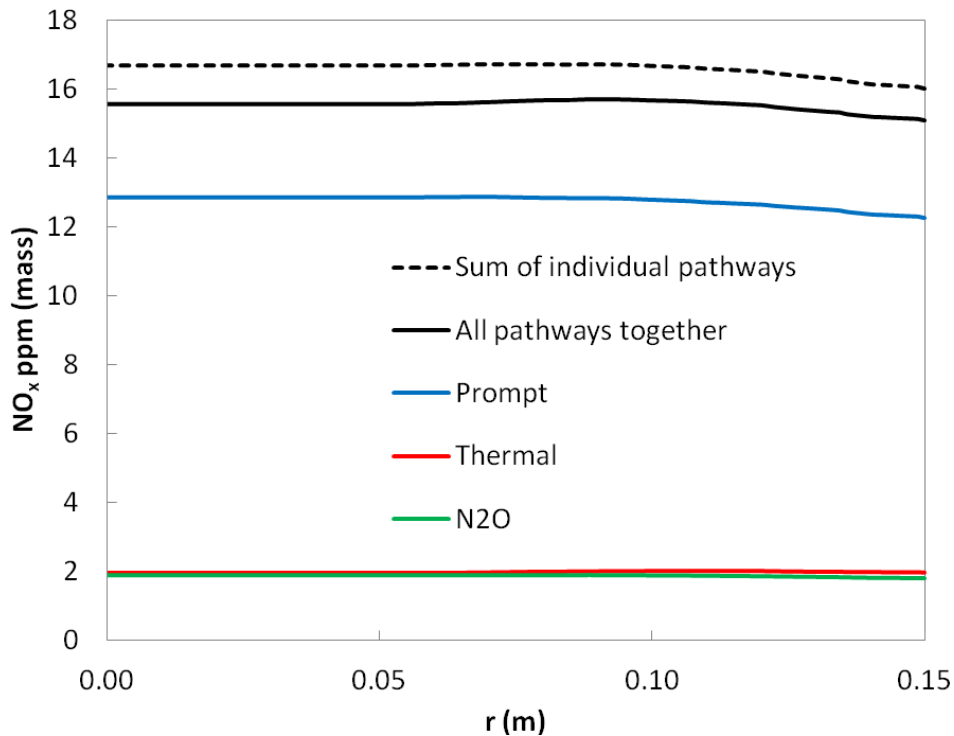
Figure 22. CFD-CRN predicted radial profiles of concentrations of NO_x ($NO+NO_2$) due to thermal (red), prompt (blue) and N_2O (green) pathways at 300 mm in parts per million (by mass)

Impacts of temperature fluctuations and alternative prompt-NO$_x$ chemistry

Another means of visualizing the secondary importance of the thermal pathway is by considering the impact of modeling temporal temperature fluctuations using the CFD-CRN. This is because the key reaction for the thermal pathway, Reaction 1, has a high activation energy of 316 kJ mol^{-1} or 75.5 kcal mol^{-1}, meaning that temperature increases have a large impact on reaction rate. **Figure 23** shows the impact of temporal temperature fluctuation modeling on NO$_x$ concentrations. The impact is predicted to be small, with the peak NO$_x$ value rising from 26.4 ppm to 27.8 ppm, an increase of 5.3%. This means that NO$_x$-forming reactions with high activation energies, such as those in the thermal pathway, are of secondary importance for this type of burner configuration operated in diffusion mode. It is expected that in premixed mode, the thermal pathway is more dominant.
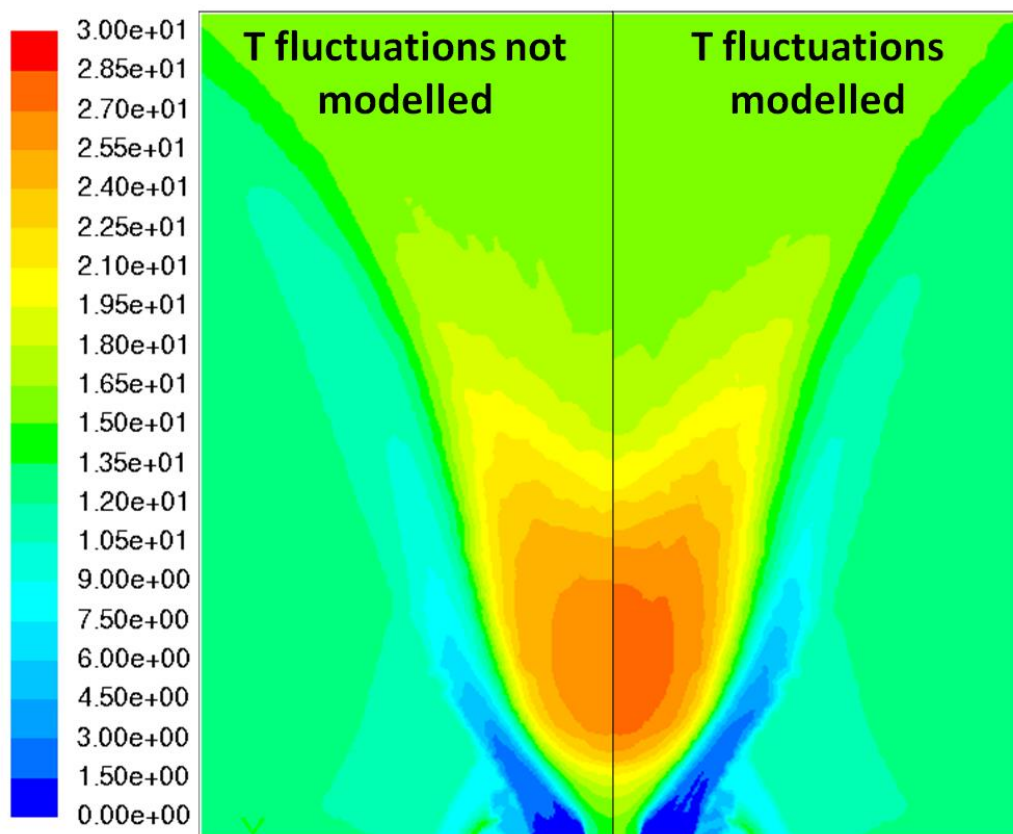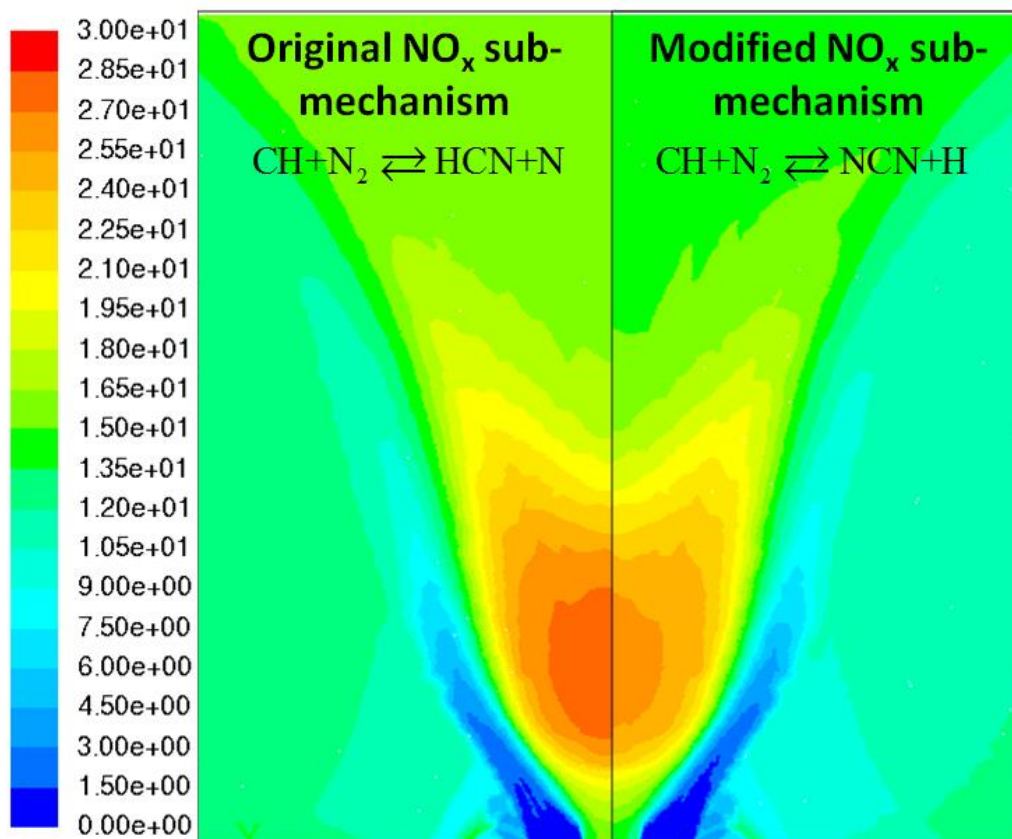
Figure 23. Impact on predicted NO_x concentration of modeling temporal temperature fluctuations in the CFD-CRN method (in ppm by mass). Refer to **Figure 6** for temperature contour plot.

The final analysis performed in this work concerns the impact of an alternative prompt reaction pathway. Recent work has suggested that the most important reaction for $CH-N_2$ combination is Reaction 8, in which NCN is the key intermediate [43,44] as shown in Table 3, as opposed to Reaction 3, in which HCN is formed. The impact on NO predictions due to the replacement of Reaction 3 in the CNRS NO_x sub-mechanism[35] with Reaction 8, and the addition of Reaction 9 to Reaction 12, with rate constant parameters as described in reference [45], was examined. The impacts on NO_x and HCN concentrations, in ppm by mass, are shown in **Figure 24** and **Figure 25**, respectively. NO_x concentrations are predicted to decrease slightly, with a decrease in peak value of 7%, due to the use of the NCN-intermediate prompt pathway. HCN concentrations are seen to be affected in high-temperature regions only, where there is a 24% decrease in peak value. Outside this area, HCN concentrations are largely unaffected. This analysis suggests that judicious choice of prompt NO pathway reactions has a non-negligible impact on predicted NO_x profiles. However for this burner configuration, regardless of whether HCN or NCN is chosen as the dominant intermediate for prompt NO, this pathway is still responsible for over 70% of NO_x present in the post-flame region.

Table 3. Important reactions and rate constant parameters for alternative prompt NO pathways

Reaction	A	n	E_a	
Original mechanism[35]				
$CH+N_2 \rightarrow HCN+N$	4.80×10^{11}	0	13600	**Reaction 3**
Modified mechanism[45]				
$CH+N_2 \rightarrow NCN+H$	3.120×10^9	0.880	21130	**Reaction 8**
$NCN+H \rightarrow HCN+N$	1.89×10^{14}	0	8425	**Reaction 9**
$NCN+O \rightarrow CN+NO$	2.55×10^{13}	0.15	-34	**Reaction 10**
$NCN+OH \rightarrow HCN+NO$	4.69×10^{10}	0.44	4000	**Reaction 11**

NCN+O$_2$ $\rightleftharpoons$ NCO+NO	3.80x10^9	0.51	24590	**Reaction 12**

Figure 24. Impact on predicted NO$_x$ concentration of replacing HCN with NCN as the key intermediate in the prompt NO pathway (in ppm by mass).
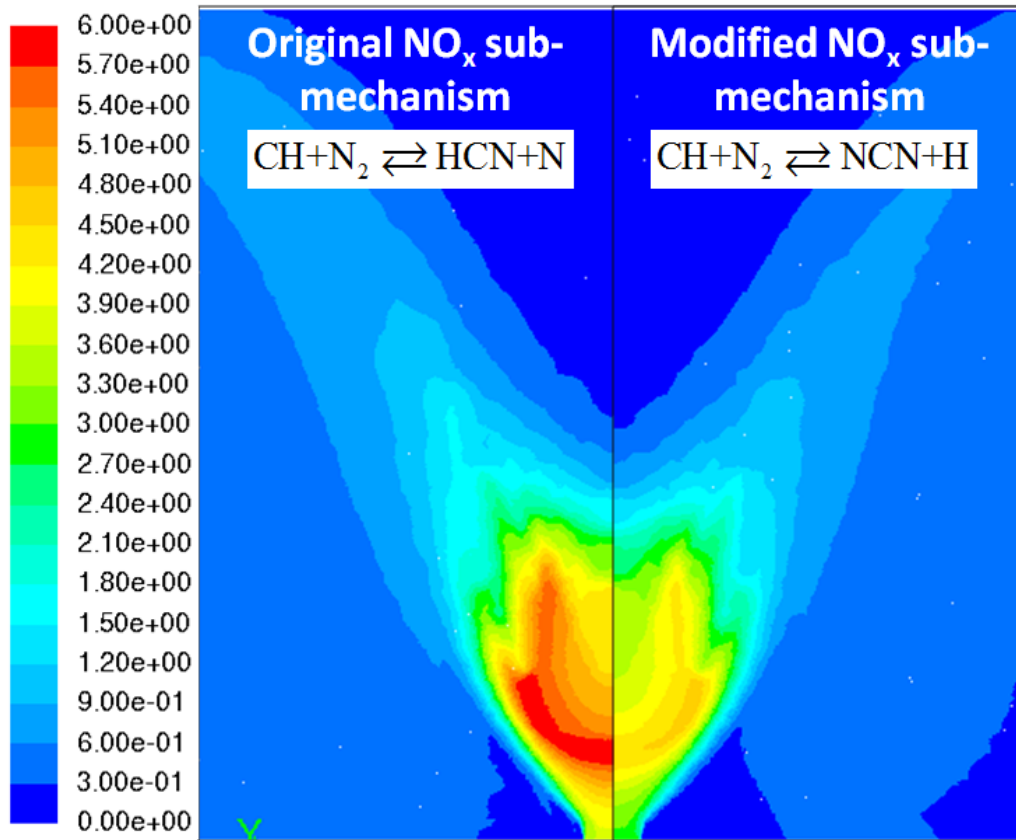
Figure 25. Impact on predicted HCN concentration of replacing HCN with NCN as the key intermediate in the prompt NO pathway (in ppm by mass).

Conclusions

A steady-state 3D CFD simulation of the S09c laboratory combustor using standard numerical techniques was experimentally validated and used as the basis for generating a CRN using the CFD-CRN method. Two CFD models were created, which differ in their handling of pressure-velocity coupling and discretization of the momentum equation. Solution B, which uses SIMPLE coupling and second-order upwind discretization of the momentum equation, was generally found to give better results. The CFD models of a 45° sector of the combustor employs standard numerical techniques and includes the following sub-models: steady-state k-ω SST turbulence, P1 radiation, finite-rate eddy-dissipation turbulence-chemistry interaction, and three-step methane combustion mechanism.

44

Size-independence studies on the CFD-CRN method determined that 5000+ PSRs were needed to adequately capture pollutant formation in the complex recirculating flow field present in S09c. This is due to the strongly swirling nature of the flame, which induces very large spatial temperature gradients. These high gradient regions are very important for reactivity and failure to model them with sufficient PSRs results in local and global under-prediction of CO.

The method was validated against experimental (mean) values of CH_4, O_2, CO_2, H_2O and CO. CFD-CRN predictions for CH_4, O_2, CO_2 and H_2O were of similar accuracy to those of steady-state CFD, except very near the burner face, where CFD-CRN predictions are of lower accuracy. This is explained by the presence of high velocity and temperature gradients in these regions, which may require much smaller, and therefore many more, PSRs. Errors due to this effect decrease downstream of the burner face. CFD-CRN predictions of CO mass fraction compare favorably to state-of-the-art CFD predictions and are seen to adequately capture high concentrations in the IRZ, as well as non-zero values in the ERZ. Deviations in CFD-CRN predictions from experimental values coincide with deviations in CFD-predicted temperature field. This indicates the need for a more detailed kinetic mechanism in the CFD simulation. While experimental NO_x data was not available for this exact flame configuration, comparison of CFD-CRN-predicted NO_x contours for $S_{0,th} = 0.9$ show satisfactory qualitative agreement with experimental measurements for $S_{0,th} = 0.7$ and $S_{0,th} = 1.4$.

The CFD-CRN method was used to study the locations and chemical pathways by which pollutant formation occurs in S09c. CO formation is concentrated in the shear layer where low-temperature incoming fuel-air streams meet and mix with the high-temperature IRZ. It is slowly consumed by oxidation to CO_2 in the high-temperature post-flame IRZ. NO_x formation is more complex and required the consideration of four widely-accepted reaction pathways; thermal, prompt, N_2O and NO_2. The relative importance of these pathways at each location within the flame was determined by isolating and deactivating each pathway in turn and examining the overall effect of NO_x rate of production. This type of analysis is inherently mechanism-dependent since it involves deactivating specific reactions that may

or may not be present in all NO_x sub-mechanisms. The analysis found that the highest-temperature regions within the IRZ are most important for NO_x formation, as expected. However, the prompt pathway at these high-temperature locations is of much greater importance than the thermal pathway. The analysis also found the choice of HCN or NCN as the main product of the $CH+N_2$ reaction in the NO_x sub-mechanism had a small but noticeable impact on overall NO_x prediction. Overall throughout the volume of this particular combustion zone, the prompt pathway is responsible for 77% of NO_x leaving the modeled system, with 12% due to thermal and 11% due to N_2O intermediate. Significant NO_x reburning occurs in the low temperature fuel-air jets immediately adjacent to the IRZ.

Calculation time for the 5551-PSR CRN was 2 hours 21 minutes using KPPSMOKE on one processor. Calculation time for the steady-state CFD simulation on which the CFD-CRN method is based was about 48 hours on 24 processors (3 GHz). In summary the CFD-CRN method will help enhance the combustor design process, giving better understanding of the interplay of geometrical features, flow field and emissions production.

Acknowledgments

References

1.   MIT *MIT Study on the Future of Natural Gas*; Massachusetts Institute of Technology: Cambridge, MA, 2011.
2.   IEA *Golden Rules for a Golden Age of Gas*; International Energy Agency: Paris, France, 2012.
3.   Falcitelli, M.; Pasini, S.; Tognotti, L., Modelling practical combustion systems and predicting NOx emissions with an integrated CFD based approach. *Computers & Chemical Engineering* **2002,** *26* (9), 1171-1183.
4.   Falcitelli, M.; Tognotti, L.; Pasini, S., An algorithm for extracting chemical reactor network models from CFD simulation of industrial combustion systems. *Combustion Science and Technology* **2002,** *174* (11-2), 27-42.

5. Frassoldati, A.; Frigerio, S.; Colombo, E.; Inzoli, F.; Faravelli, T., Determination of NO_x emissions from strong swirling confined flames with an integrated CFD-based procedure. *Chemical Engineering Science* **2005,** *60* (11), 2851-2869.

6. (a) Drennan, S. A., Flowfield-Derived Equivalent Reactor Networks for Accurate Chemistry Simulation in Gas Turbine Combustors, GT2009-59861. In *ASME Turbo Expo 2009*, Orlando, FL, 2009; (b) Lebedev, A. B.; Secundov, A. N.; Starik, A. M.; Titova, N. S.; Schepin, A. M., Modeling study of gas-turbine combustor emission. *Proc. Combust. Inst.* **2009,** *32*, 2941-2947.

7. Fichet, V.; Kanniche, M.; Plion, P.; Gicquel, O., A reactor network model for predicting NO_x emissions in gas turbines. *Fuel* **2010,** *89*, 2202-2210.

8. Starik, A. M.; Lebedev, A. B.; Savel'ev, A. M.; Titova, N. S.; Leyland, P., Impact of Operating Regime on Aviation Engine Emissions: Modeling Study. *J. Propul. Power* **2013,** *29* (3), 709-717.

9. Monaghan, R. F. D.; Tahir, R.; Cuoci, A.; Bourque, G.; Füri, M.; Gordon, R. L.; Faravelli, T.; Frassoldati, A.; Curran, H. J., Detailed Multi-dimensional Study of Pollutant Formation in a Methane Diffusion Flame. *Energy & Fuels* **2012,** *26* (3), 1598-1611.

10. Cuoci, A.; Frassoldati, A.; Stagni, A.; Faravelli, T.; Ranzi, E.; Buzzi-Ferraris, G., Numerical Modeling of NOx Formation in Turbulent Flames Using a Kinetic Post-processing Technique. *Energy & Fuels* **2012,** *27* (2), 1104-1122.

11. Frassoldati, A.; Cuoci, A.; Faravelli, T.; Ranzi, E.; Colantuoni, S.; Di Martino, P.; Cinque, G., EXPERIMENTAL AND MODELING STUDY OF A LOW NOX COMBUSTOR FOR AERO-ENGINE TURBOFAN. *Combustion Science and Technology* **2009,** *181* (3), 483-495.

12. Schneider, C.; Repp, S.; Sadiki, A.; Dreizler, A.; Janicka, J.; Meier, W.; Noll, B.; Bockhorn, H.; Leuckel, W.; Lenze, B.; Schmittel, P.; Schulz, C.; Wolfrum, J., Confined TECFLAM swirl burner: Experimental investigations and numerical simulations. In *5th International Workshop on Measurement and Computation of Turbulent Non-Premixed Flames*, Mbiock, A.; Roekaerts, D.; Barlow, R. S., Eds. Delft, The Netherlands, 2000.

13. Schmittel, P.; Gunther, B.; Lenze, B.; Leuckel, W.; Bockhorn, H., Turbulent swirling flames: Experimental investigation of the flow field and formation of nitrogen oxide. *Proc. Combust. Inst.* **2000,** *28*, 303-309.

14. Landenfeld, T.; Kremer, A.; Hassel, E. P.; Janicka, J.; Schäfer, T.; Kazenwadel, J.; Schulz, C.; Wolfrum, J., Laser-diagnostic and numerical study of strongly swirling natural gas flames. *Symposium (International) on Combustion* **1998,** *27* (1), 1023-1029.

15. Böckle, S.; Kazenwadel, J.; Kunzelmann, T.; Shin, D. I.; Schulz, C., Single-shot laser-induced fluorescence imaging of formaldehyde with XeF excimer excitation. *Applied Physics B: Lasers and Optics* **2000,** *70* (5), 733-735.

16. Yang, W.; Zhang, J., Simulation of swirling turbulent combustion in the TECFLAM combustor. *Computers & Chemical Engineering* **2008,** *32* (10), 2280-2289.

17. Yang, W.; Zhang, J., Simulation of methane turbulent swirling flame in the TECFLAM combustor. *Applied Mathematical Modelling* **2009,** *33* (6), 2818-2830.

18. Meier, W.; Keck, O.; Noll, B.; Kunz, O.; Stricker, W., Investigations in the TECFLAM swirling diffusion flame: Laser Raman measurements and CFD calculations. *Applied Physics B: Lasers and Optics* **2000,** *71* (5), 725-731.

19. Ayache, S. Simulations of turbulent swirl combustors. Cambridge University, Cambridge, 2011.

20. Kuenne, G.; Ketelheun, A.; Janicka, J., LES modeling of premixed combustion using a thickened flame approach coupled with FGM tabulated chemistry. *Combustion and Flame* **2011,** *158* (9), 1750-1767.

21. Freitag, M.; Janicka, J., Investigation of a strongly swirled unconfined premixed flame using LES. *Proc. Combust. Inst.* **2007,** *31* (1), 1477-1485.

22. Böckle, S.; Kazenwadel, J.; Kunzelmann, T.; Schulz, C., Laser-diagnostic multi-species imaging in strongly swirling natural gas flames. *Applied Physics B: Lasers and Optics* **2000,** *71* (5), 741-746.

23. Keck, O.; Meier, W.; Stricker, W.; Aigner, M., Establishment of a Confined Swirling Natural Gas/Air Flame as a Standard Flame: Temperature and Species Distributions from Laser Raman

Measurements. *Combustion Science and Technology* **2002,** *174* (8), 117-151.

24.   Böckle, S.; Kazenwadel, J.; kunzelmann, T.; Shin, D.-I.; Schulz, C.; Wolfrum, J., Simultaneous single-shot laser-based imaging of formaldehyde, OH, and temperature in turbulent flames. *Proc. Combust. Inst.* **2000,** *28* (1), 279-286.

25.   Siemens NX - Transforming the process of innovation. http://www.plm.automation.siemens.com/en_us/products/nx/ (accessed 11/04/2012).

26.   Schneider, C. Über die Charakterisierung von Turbulenzstrukturen in verdrallten Strömungen. Technischen Universität Darmstadt, Darmstadt, 2003.

27.   ANSYS, ANSYS FLUENT 14.0 Theory Guide. **2011**.

28.   Cheng, P., Two-Dimensional Radiating Gas Flow by a Moment Method. *AIAA Journal* **1964,** *2*, 1662-1664.

29.   Siegel, R.; Howell, J. R., *Thermal Radiation Heat Transfer*. Hemisphere Publishing Corporation: Washington DC, 1992.

30.   Dryer, F. L.; Glassman, I., High-temperature oxidation of CO and CH4. *Symposium (International) on Combustion* **1973,** *14* (1), 987-1003.

31.   Westbrook, C. K.; Dryer, F. L., SIMPLIFIED REACTION-MECHANISMS FOR THE OXIDATION OF HYDROCARBON FUELS IN FLAMES. *Combustion Science and Technology* **1981,** *27* (1-2), 31-43.

32.   ANSYS, *ANSYS FLUENT 14.0 UDF Manual*. 2011.

33.   Healy, D.; Donato, N. S.; Aul, C. J.; Petersen, E. L.; Zinner, C. M.; Bourque, G.; Curran, H. J., n-Butane: Ignition delay measurements at high pressure and detailed chemical kinetic simulations. *Combustion and Flame* **2010,** *157* (8), 1526-1539.

34.   Lowry, W.; de Vries, J.; Krejci, M.; Petersen, E.; Serinyel, Z.; Metcalfe, W.; Curran, H.; Bourque, G., Laminar Flame Speed Measurements and Modeling of Pure Alkanes and Alkane Blends at Elevated Pressures. *Journal of Engineering for Gas Turbines and Power* **2011,** *133* (9), 091501-9.

35.   Sivaramakrishnan, R.; Brezinsky, K.; Dayma, G.; Dagaut, P., High pressure effects on the mutual sensitization of the oxidation of NO and CH_4-C_2H_6 blends. *Phys. Chem. Chem. Phys.* **2007,** *9* (31), 4230-4244.

36.   Stagni, A.; Cuoci, A.; Frassoldati, A.; Faravelli, T.; Ranzi, E., A fully coupled, parallel approach for the post-processing of CFD data through reactor network analysis. *Computers and Chemical Engineering* **2013,** *60* (197-212).

37.   Correa, S. M., A Review of NO_x Formation Under Gas-Turbine Combustion Conditions. *Combustion Science and Technology* **1993,** *87* (1), 329 - 362.

38.   Kuo, K. K., *Principles of Combustion*. John Wiley & Sons, Inc.: Hoboken, N.J., 2005.

39.   Fenimore, C. P., Formation of nitric oxide in premixed hydrocarbon flames. *Symposium (International) on Combustion* **1971,** *13* (1), 373-380.

40.   Malte, P. C.; Pratt, D. T., ROLE OF ENERGY-RELEASING KINETICS IN NOX FORMATION - FUEL-LEAN, JET-STIRRED CO-AIR COMBUSTION. *Combustion Science and Technology* **1974,** *9* (5-6), 221-231.

41.   Bozzelli, J. W.; Dean, A. M., O+NNH - A POSSIBLE NEW ROUTE FOR NOX FORMATION IN FLAMES. *Int. J. Chem. Kinet.* **1995,** *27* (11), 1097-1109.

42.   Fackler, K. B.; Karalus, M. F.; Novosselov, I. V.; Kramlich, J. C.; Malte, P. C., Experimental and Numerical Study of NO_x Formation From the Lean Premixed Combustion of CH4 Mixed With CO_2 and N_2. *Journal of Engineering for Gas Turbines and Power* **2011,** *133* (12), 121502-7.

43.   Moskaleva, L. V.; Xia, W. S.; Lin, M. C., The CH+N2 reaction over the ground electronic doublet potential energy surface: a detailed transition state search. *Chemical Physics Letters* **2000,** *331* (2–4), 269-277.

44.   Harding, L. B.; Klippenstein, S. J.; Miller, J. A., Kinetics of CH + N2 Revisited with Multireference Methods. *The Journal of Physical Chemistry A* **2008,** *112* (3), 522-532.

45.   Sepman, A. V.; Mokhov, A. V.; Levinsky, H. B., The effects of hydrogen addition on NO formation in atmospheric-pressure, fuel-rich-premixed, burner-stabilized methane, ethane and propane

flames. *International Journal of Hydrogen Energy* **2011,** *36* (7), 4474-4481.

Nomenclature

ACM = algebraic concentration moment

C^3 = Combustion Chemistry Centre

CFD = computational fluid dynamics

CMC = conditional moment closure

CNRS = Centre National de la Recherche Scientifique

CRN = chemical reactor network

DLR = Deutsches Zentrum für Luft- und Raumfahrt (German Aerospace Centre)

EBU = eddy break-up

EDC = eddy dissipation concept

ERZ = external recirculation zone

FGM = flamelet generated manifold

IRZ = inner recirculation zone

KPPSMOKE = Kinetic Post Processor

LES = large eddy simulation

LDV = laser Doppler velocimetry

LNG = liquefied natural gas

Nm^3 hr^{-1} = Normal cubic meters per hour, measured at normal metric conditions (1 atm, 25 °C)

PDF = probability distribution function

PVC = precessing vortex core

RANS = Reynolds averaged Navier-Stokes

SIMPLE = semi-implicit method for pressure-linked equations

SST = shear stress transport

TUD = Technische Universität Darmstadt

Lowercase letters

c_p = specific heat capacity (J kg^{-1} K^{-1})

h = enthalpy (J kg^{-1})

h_c = convective heat transfer coefficient (W m^{-2} K^{-1})

k = turbulent kinetic energy (m^2 s^{-2}) or thermal conductivity (W m^{-1} K^{-1}) or kinetic reaction rate constant

l_{cell} = cell length-scale (m)

$\dot{m}_{adv}$ = advective mass flow rate (kg s^{-1})

$\dot{m}_{diff,t}$ = turbulent diffusive mass flow rate (kg s^{-1})

n = number of guide vanes in swirler

p = pressure (Pa, MPa, atm or bar) or probability

r = chemical reaction rate (kg m^{-3} s^{-1} or kmol m^{-3} s^{-1})

r_0 = inner radius of swirler (mm)

u = axial velocity (m s^{-1})

v = radial velocity (m s^{-1})

w = tangential velocity (m s^{-1})

Uppercase letters

A = pre-exponential factor or area (m^2)

B = axial width of swirler annular channel (mm)

C = constant

$D_{m,t}$ = turbulent mass diffusivity (m^2 s^{-1})

E_a = activation energy (kJ $kmol^{-1}$)

N = number

$Pe_{m,t}$ = Peclet number for turbulent mass transfer

R = ideal gas constant (J kg^{-1} K^{-1})

R_0 = outer radius of swirler (mm)

$S_{0,th}$ = theoretical swirl number

Sc_t = turbulent Schmidt number

T = temperature (°C or K)

T_{rms} = temporal root mean square temperature fluctuation (°C or K)

V = volume (m^3)

Y = mass fraction

Z = any property

Greek letters

α = angular position of fixed swirl block (deg) or rate exponent

β = temperature power for reaction rate constant

ε = emissivity or wall roughness or turbulent dissipation rate (m^2 s^{-3})

μ_t = turbulent viscosity (Pa s)

ν = kinematic viscosity (m^2 s^{-1})

ρ = density (kg m^{-3})

ζ = angular position of moveable swirl block (deg)

ζ_m = maximum angular position of moveable swirl block (deg)

σ_T^2 = temperature variance (K^2)

ω = specific dissipation rate (s^{-1})

ξ^{*3} = EDC volume fraction

∇T = temperature gradient (K m^{-1})